이학석사 학위논문

고효율 촉매 활성을 지닌 나노 물질의 합성 및 특성연구

Fabrication and Characterization of Nanostructured Materials with High Catalytic Activity

2016 년 8 월

서울대학교 대학원

화학부 물리화학전공

이 혜 리

A Master' Dissertation

Fabrication and Characterization of Nanostructured Materials with High Catalytic Activity

By Hyeri Lee

Supervisor: Professor Du-Jeon Jang

Major: Physical chemistry

School of Chemistry

Graduate School of Seoul National University

August 2016

고효율 촉매 활성을 지닌 나노 물질의 합성 및 특성연구

Fabrication and Characterization of Nanostructured Materials with High Catalytic Activity

지도교수 장 두 전

이 논문을 이학석사 학위논문으로 제출함

2016 년 8 월

서울대학교 대학원
화학부 물리화학 전공
이 혜 리

이혜리의 이학석사학위논문을 인준함
2016 년 6월

위 원 장 홍 병 희 (인)
부위원장 장 두 전 (인)
위 원 정 택 동 (인)

Abstract of Dissertation

In this dissertation, fabrication, characterization, and application of nanostructured material catalysts are discussed from the point of view of physical and materials chemistry. Brief overviews of the chapter 1 and 2 in this dissertation are shown below.

In chapter 1, well-defined uniform anatase TiO_2 nanotube arrays with the predominant exposure of the highly energetic {001} facets have been prepared via a two-step anodic oxidation process of Ti foil. With the increase of the first-anodization time (up to 11 h) and/or the NH_4F concentration, the exposure degree of the {001} facets, as well as the photocatalytic activity, crystallite sizes, and crystallinity, of prepared TiO_2 nanotube arrays has been found to increase. Especially, the photocatalytic activity of TiO_2 nanotube arrays increases in accordance with increase in the exposure degree of the {001} facets, suggesting that the highly energetic {001} facets enhance the photocatalytic activity of TiO_2 nanotube arrays on a large scale.

In chapter 2, morphology-controlled Ag/Au nanocomposite have been fabricated facilely via a modified galvanic replacement reaction using Ag nanocubes as sacrificial templates. The morphologies of Ag/Au nanaocomposites have been readily controlled by adjusting the temperature of the galvanic reaction. Among the prepared samples, Ag/Au nanocomposites fabricated at 85 ^oC show the most efficient catalytic performances as their

largest nanocavities are surrounded by the most porous walls.

Keywords: Anatase TiO_2, Anodization, Degradation, Hollow structure, Nanobox, Nanotube array, Reactive facet

Student Number: 2013-22934

Table of Contents

List of Figures and Tables

min. (b) The fluorescence intensity at 425 nm of TAOH versus the irradiated time with indicated TNT arrays.

Figure 1-S1. FESEM image of collapsed TNT-17.

Figure 1-S2. FESEM images of (a) TNT-2 (0.5%), (b) TNT-2 (1.0%), and (c) TNT-2 (2.5%). Each scale bar indicates 200 nm.

Figure 1-S3. HRXRD patterns of indicated TNT arrays. The standard diffraction pattern of anatase TiO_2 is also shown in the bottom.

Figure 1-S4. High-resolution XPS spectra of F 1s for indicated first-anodized TNT arrays and calcined TNT-11.

Figure 1-S5. High-resolution XPS spectra of (left) O 1s and (right) Ti 2p for (top) TNT-2 and (bottom) TNT-11.

Figure 1-S6. First-order kinetics, $\ln(C/C_0)$ versus the irradiation time, of phenol(aq) degradation in the presence of indicated TNT arrays.

Figure 1-S7. First-order kinetic plots for the photocatalytic degradation of 10 μM RhB(aq) in the presence of indicated TNT arrays.

Figure 1-S8. First-order kinetics, $\ln(C/C_0)$ versus the irradiation time, of RhB(aq) degradation via (red) TNT-2 and (green) TNT-11 in (open) the absence and (closed) the presence of sodium sulfite.

Table 1-S1. Average crystallite sizes (d), (004)/(101) intensity ratios (R), and rate constants (k) for the catalytic degradation of 10 μM RhB(aq) via TNT arrays under irradiation by a 300 W Xe lamp.

Figure 2-1. Illustration for the temperature-controlled morphology evolution of Ag/Au nanocomposites.

Figure 2-2. TEM images of (a) Ag_{pr}, (b) Ag/Au_{25} (c) Ag/Au_{55}, and (d) Ag/Au_{85}.

Figure 2-3. STEM images, EDX elemental maps, and area-normalized line-scanned elemental intensity profiles of (a) Ag_{pr}, (b) Ag/Au_{25}, (c) Ag/Au_{55}, and (d) Ag/Au_{85}.

Figure 2-4. Maximum-normalized surface-plasmon resonance spectra of indicated nanocatalysts in water.

Figure 2-5. Absorption spectra at 25 °C of 11 μM RhB(aq) in the presence of 1.3 mM KBH_4, measured at elapsed times indicated in the units of min after addition of (a) Ag_{pr}, (b) Ag/Au_{25}, (c) Ag/Au_{55}, and (d) Ag/Au_{85}.

Figure 2-6. $\ln(A/A_0)$ vs t for the catalytic degradation of 11 μM RhB(aq) via (a) Ag_{pr} (b) Ag/Au_{85} in the presence of 1.3 mM KBH_4 at indicated temperatures.

Figure 2-7. (a) Arrhenius plots for the catalytic reduction reaaction of 11 μM RhB(aq) via indicated nanocatalysts in the presence of 1.3 mM KBH_4. (b) The compensation law plot of the frequency factors and the activiation energies extracted from the Arrhenius plots.

Table 2-1. Observed rate constants (k_{obs}) at 25 °C, induction time (t_0) at 25 °C, activation energies (Ea), frequency factors (A), activation enthalpies ($\Delta H^{\ddagger}$), and activation entropies ($\Delta S^{\ddagger}$) for the catalytic reduction of RhB via nanocomposites in the presence of BH_4^-.

Figure 2-S1. TEM images of (a) Ag/Au_0 and (b) Ag/Au_{105}.

Figure 2-S2. TEM images and edge-size distribution histograms of (a) Ag_{pr}, (b) Ag/Au_0, (c) Ag/Au_{25}, (d) Ag/Au_{55}, (e) Ag/Au_{85}, and (f) Ag/Au_{105}. Average edge sizes are indicated inside the histograms.

Figure 2-S3. STEM image, EDX elemental maps, and area-normalized line-scanned (along the line of the STEM image) elemental intensity profiles of Ag/Au_0.

Figure 2-S4. Maximum-normalized surface-plasmon resonance spectra of indicated nanocatalysts in water.

Figure 2-S5. Absorption spectra at 25 °C of 11 μM RhB(aq) in the presence of 1.3 mM KBH_4, measured at elapsed times indicated in the units of min after addition of (a) Ag/Au_0 and (b) Ag/Au_{105}.

Figure 2-S6. Eyring plots for the catalytic degradation reaaction of 11 μM RhB(aq) via indicated nanocatalysts in the presence of 1.3 mM KBH_4.

Chapter 1. Preparation of Anatase TiO_2 Nanotube Arrays Dominated with Highly Reactive Facets via Anodization for High Photocatalytic Performances

1. 1. Abstract

Well-defined uniform anatase TiO_2 nanotube (TNT) arrays with the predominant exposure of the highly energetic {001} facets have been prepared via a two-step anodic oxidation process of Ti foil. In order to enhance the exposure degree of the {001} facets, NH_4F has been used for a capping agent during anodization and the evolution of TNT arrays has been varied by changing the duration of anodization and the concentration of NH_4F. With the increase of the first-anodization time (up to 11 h) and/or the NH_4F concentration, the crystallite sizes, crystallinity, and exposed {001} facets of prepared TNT arrays have been found to increase. The photocatalytic activity of as-prepared TNT arrays, evaluated by monitoring the photodegradation of rhodamine B, has been found to increase in accordance with increase in the exposure degree of the {001} facets, indicating that the highly energetic {001} facets enhance the photocatalytic activity of TNT arrays on a large scale. The {001} facets of TNT arrays have been considered to provide oxidation sites extensively, which produce active oxygen species such as •OH, $•O_2^-$, and H_2O_2 upon UV irradiation. Our results have shown that •OH is the predominant highly active species for the photocatalytic degradation of organic dye pollutants via TNT arrays. We consider that this study may provide a new insight into the preparation and development of advanced photocatalytic anatase TiO_2 materials.

1. 2. Introduction

With the exponential growth of environmental contamination, the development of an ideal green technology has drawn much attention on a global scale [1,2]. As one of the most promising solutions for these problems, photocatalysis which is inexhaustibly prevalent, clean, nonhazardous, and economically viable has become a promising remediation technology [3,4]. In this regard, TiO_2 nanostructures have undoubtedly proven to be ideal photocatalysts due to their chemical inertness, long-term stability against photo and chemical corrosion, non-toxicity, and high reactivity for water splitting and the oxidative decomposition of many organic pollutants [5,6].

Anatase TiO_2, which is one of the four polymorphs of TiO_2, has been extensively investigated for wide applications in photocatalysts, sensors, Li batteries, photovoltaic cells, and so on [7-9]. The photocatalytic activity depends not only on the shapes and external surfaces of particles but also on the arrangement and coordination of surface atoms on crystal facets. Typical anatase crystals of TiO_2 are primarily dominated by the {101} facets, which are thermodynamically stable due to their low surface energy (0.44 J/m^2) [10,11]. Unfortunately, the more reactive {001} facets rapidly diminish during the crystal growth process, resulting from the minimization of the total surface free energy. Therefore, the controllable synthesis of the exposed {001} facets has become a hot research direction to improve the photocatalytic activity of anatase TiO_2 greatly [12-14]. Yang et al. has reported an important

breakthrough in the synthesis of anatase TiO_2 single crystals with a high percentage of the exposed {001} facets by using fluorine as a stabilizing agent; adsorbed fluorine ions could reduce the surface energies of facets and the exposed ratio of facets depends on differential adsorption energies [13]. On the basis of these results, it is likely to optimize the photocatalytic activity of anatase TiO_2 by tailoring the exposure of high-energy facets [15-17]. Anatase TiO_2 crystals with a high ratio of the exposed {001} facets have great potential in applications for solar cells, photonic and optoelectronic devices, and photocatalysts [14,18,19].

Many studies have focused on the synthesis of TiO_2 with various structures such as nanotube arrays, nanoparticles, nanorods, mesoporous spheres, nanosheets, nanowires, and micro-flowers [9,18,20,21]. In particular, well-aligned one dimensional TiO_2 nanotube (TNT) arrays have a high surface-to-volume ratio and provide a convenient method for photo-generated electrons to be transferred. Thus, the faster transport, the slower recombination, and the resulting higher charge collection ability of highly oxidative photocarriers, all of which improve photocatalyic performance enormously, can be anticipated [22]. One dimensional TiO_2 nanostructures have been synthesized using a range of techniques including sol-gel reaction, hydrothermal synthesis, microwave-assisted hydrothermal synthesis, chemical vapor deposition, electrospinning, and electrochemical anodization [23-25]. Among these techniques, the electrochemical anodization process offers some additional advantages such as the ease of fabrication, the control of morphologies, and the ability to form ordered arrays without using any templates [26,27]. TNT

arrays can be formed by electrochemical anodization in aqueous and organic electrolytes, typically fluoride-containing media.

In this work, we have prepared free-standing TNT arrays dominated with the highly energetic {001} facets via a two-step anodization process (Figure 1-1). We have tailored the TNT arrays simply by adjusting the duration of the first anodization and the concentration of NH_4F, which have controlled the exposure degree of the {001} facets. Using the prepared TNT arrays, we have also performed the photodegradation kinetics of rhodamine B, revealing that the photocatalytic activity of the TNT arrays is dependent on the {001} facets. The photoluminescence (PL) technique using terephthalic acid [28,29] has also been employed to prove the dependence of the photocatalytic activity on the exposure degree of the {001} facets of anatase TNT arrays. Thus, it has been shown that the photocatalytic activity of anatase TNT arrays can be optimized by maximizing the exposure degree of the high-energy {001} facets.

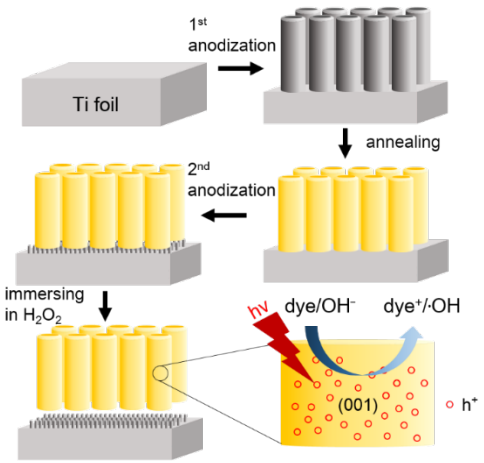

Figure 1-1. Schematic illustration for the fabrication and photocatalysis of a free-standing crystalline TNT array.

1. 3. Experimental Section

3.1 Materials and preparation

3.1.1 Materials. Chemicals were used as received: Ti foil (s, 0.25 mm thick, ≥99.7%), NH_4F (s, ≥98%), Pt gauze (s, 100 mesh, ≥99.9%), sodium hydroxide (s, >97%), and terephthalic acid (TA, s, 98%) from Sigma-Aldrich; ethylene glycol (EG, *l*, ≥99%) from Daejung Chemicals; H_2O_2 (aq, 34%) from Samchun Pure Chemicals; phenol (s, 99%) and sodium sulfite (s, 98%) from Alfa Aesar; rhodamine B (RhB, s) from Wako Pure Chemicals. Ultrapure deionized water (>17 MΩ cm) from a Millipore Milli-Q system was used throughout the experiments.

3.1.2 Preparation. Highly ordered TiO_2 NT arrays dominated with highly energetic {001} facets were prepared by potentiostatic anodization in a two-electrode electrochemical cell [30,31]. All the anodization experiments were carried out at room temperature using commercial Ti foil (1.5 x 1.5 cm^2) as the anode and Pt gauze (2.5 x 2.5 cm^2) as the cathode, and the voltage was applied by an Agilent Technologies E3612A DC power supply. Prior to anodization, Ti foil was ultrasonically washed with acetone, ethanol, and distilled water, and then dried with a purging N_2 gas. To get stable free-standing nanotube arrays, the anodization process was divided into two steps using an electrolyte solution containing typically 0.5 wt% NH_4F and 2.5 vol% water in EG. At the first step, the Ti foil was anodized at 50 V for several hours and ultrasonically washed with ethanol and acetone to remove electrolytes and debris. Then, as-anodized amorphous TiO_2 was converted into the

anatase phase by annealing at 500 °C for 2 h. The annealed sample was anodized again under the same anodizing conditions for 30 min in order to detach TNT arrays from the Ti foil. After these two steps, the anodized sample was immersed in a 34% H_2O_2 solution for 12 h. As a result, the TNT arrays were separated from the Ti foil to form a free-standing membrane. To adjust the exposure degree of the {001} facets, the duration of the first anodization was varied from 2 to 17 h to produce diverse types of TNT-x (x = 2, 7, 9, 11, and 17), where x represents the duration of the first anodization in the unit of h. To investigate the effect of the concentration of NH_4F, TNT-2 (1.0%) and TNT-2 (2.5%) were also prepared by carrying out the two-step anodization processes at the NH_4F concentrations of 1.0 and 2.5 wt%, respectively.

3.2 Characterization and evaluation

3.2.1 General. Transmission electron microscopy (TEM) images, selected-area electron diffraction (SAED) patterns, and fast Fourier-transform (FFT) patterns were obtained using a FEI Tecnai F20 microscope, and field emission scanning electron microscopy (FESEM) images were measured with a ZEISS MERLIN Compact microscope. High-resolution X-ray diffraction (HRXRD) patterns were recorded using a Bruker D8 DISCOVER diffractometer (Cu Kα radiation, $\lambda = 0.154178$ nm). X-ray photoelectron spectroscopy (XPS) spectra were collected using a Thermo Scientific Sigma Probe ESCA spectrometer with an X-ray source of Al K_α and the measured binding energies were calibrated with the C 1s peak at 284.5 eV of contaminated carbon. Absorption spectra were measured with a Scinco S3100 UV-vis spectrophotometer, and emission spectra were obtained using a fluorometer

consisting of a 75 W Acton Research XS 432 Xe lamp with an Acton Research Spectrapro 150 monochromator of 0.15 m and an Acton Research PD438 photomultiplier tube attached to an Acton Research Spectrapro 300 monochromator of 0.30 m. All the measurement were conducted at room temperature.

3.2.2 Measurement of photocatalytic activity. The evaluation of the photocatalytic performances of as-prepared samples were performed at ambient conditions with RhB as the target organic pollutant. Photocatalytic experiments were carried out in a round-bottom quartz vessel. Prior to illumination, a suspension containing 5 mg of TNT arrays and 30 mL of 10 μM RhB(aq) was continuously stirred in the dark for 1 h to ensure the adsorption-desorption equilibrium of RhB on the nanocatalyst surface. The concentration of RhB in the reaction mixture at this point was used as the initial value for the adsorption and the kinetic treatment of photodegradation. The reaction mixture was placed 30 cm away from a 300 W Schoeffel LPS 255 HR xenon arc lamp, and its aliquots were taken at scheduled intervals during irradiation and centrifuged (12 000 rpm, 10 min) to separate the supernatant, whose UV/vis absorption spectrum was then recorded to monitor the concentration of remnant RhB. The photocatalytic activity was also investigated by monitoring phenol photo-degradation; the experimental procedure was the same except that 10 μM RhB(aq) was replaced by 30 mg L^{-1} phenol(aq). To compare the amount of holes in TNT-11 with that in TNT-2, some photocatalytic experiments were carried out with and without the addition of 100 mg sodium sulfite as a hole scavenger in a reaction mixture.

3.2.3 Analysis of hydroxyl radicals. The analysis of hydroxyl radicals formed on the surface of photoilluminated TNT arrays was performed by the photoluminescence technique using TA as the probing molecule, which readily reacted with a hydroxyl radical to produce a highly fluorescent product, 2-hydroxyterephthalic acid (TAOH) [28,29]. Typically, 0.5 mg of a photocatalyst was suspended into 30 mL of an aqueous solution containing 2 mM NaOH and 0.5 mM TA in a quartz reactor. Prior to a photoreaction, the suspension was magnetically stirred in the dark for 1 h to get the adsorption-desorption equilibrium. Experimental procedures were similar to those of photocatalytic activity except that RhB was replaced by TA with NaOH. The PL spectra of generated TAOH were measured using a JASCO FP-8300 fluorescence spectrometer with excitation at 315 nm. After every light irradiation for 15 min, the reaction solution was used to measure the increase of PL intensity at 425 nm.

1. 4. Results and Discussion

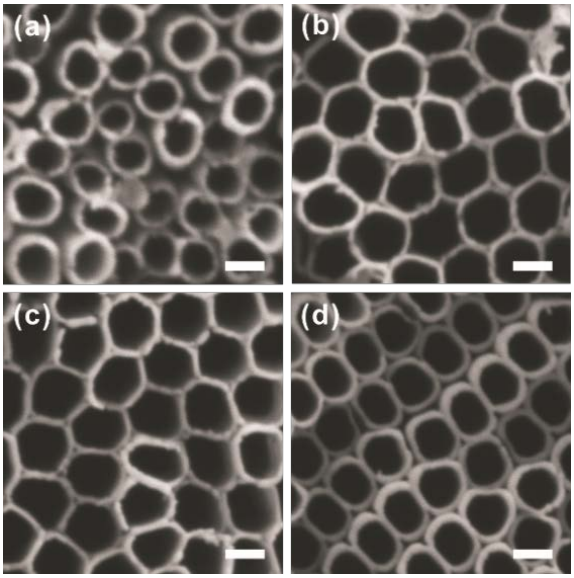

Figure 1-2. FESEM images of (a) TNT-2, (b) TNT-7, (c) TNT-11, and (d) TNT-17. Each scale bar indicates 100 nm.

Figure 1-2 shows the surface morphologies of TNT arrays prepared under a constant anodizing voltage of 50 V. Average outer (inner) diameters for TNTs of TNT-2, TNT-7, TNT-11, and TNT-17 prepared by the first anodization for 2, 7, 11, and 17 h, respectively, have been found as 97 (70), 145 (122), 152 (130), and 134 (111) nm, respectively. Thus the average wall thickness values of TNT-2, TNT-7, TNT-11, and TNT-17 have been estimated as 14, 11, 9, and 11 nm, respectively. In addition, the lengths of the TNTs have showed a tendency to increase with the duration increment of the first anodization; the average lengths of TNT-2, TNT-7, TNT-11, and TNT-17 have been estimated as 13, 20, 27, and 21 μm, respectively. As

the anodization duration was increased from 11 to 17 h, the average outer (inner) diameter and the average length were reduced by 18 (19) nm and 6 μm, respectively. As illustrated in the top-view FESEM image of Figure 1-S1, some of TNT-17 near the tube mouths have been broken up due to the high electrochemical etching rate near the top of the TNT array [23]. This is considered to result from a fluoride concentration much higher at the tube mouth than at the tube bottom. With the increase of the first anodization time, the nanotubes were chemically etched severely, resulting in the crack and exfoliation of nanotubes. Meanwhile, Figure 1-S2 shows the evolution of the morphologies of the TNT arrays as a function of the NH_4F concentration ranging from 0.5 wt% to 2.5 wt%. The average outer (inner) diameters of TNT-2 prepared at the NH_4F concentrations of 0.5, 1.0, and 2.5wt% have been found as 97 (70), 124 (101), and 129 (107) nm, respectively. Thus, it has been suggested that the increase of the NH_4F concentration enhances the dissolution of TiO_2, subsequently increasing the diameters of TNTs.

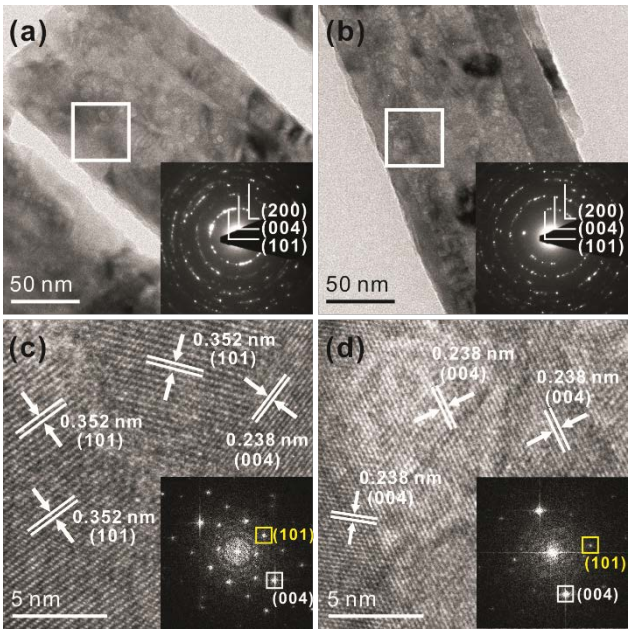

Figure 1-3. TEM images (whose insets show SAED patterns taken from squares) of (a) TNT-2 and (b) TNT-11 and HRTEM images (whose insets show FFT patterns) of (c) TNT-2 and (d) TNT-11.

The clear contrast of each TEM image of Figure 1-3a and b indicates that each TNT has a tubular structure indeed. The SAED patterns in the insets of Figure 1-3a and 3b exhibit that both TNT-2 and TNT-11 have the diffraction rings of the (101), (004), and (200) planes, suggesting that both TNTs correspond well to the polycrystalline phase of the anatase TiO_2. The HRTEM image of Figure 1-3c indicates that the average d-spacing values of 0.352 and 0.238 nm observed in TNT-2 agree very well with the standard spacings of 0.351 and 0.238 nm between the (101) planes and (004) planes of the anatase TiO_2 lattice (JCPDS 21-1272), respectively. It has been reported that the order of the average surface energies is {001} (0.90 J m^{-2}) > {010} (0.53 J m^{-2}) >

{101} (0.44 J m^{-2}) [13,32]. Therefore, TNT-2 shows (101) planes mainly, which are energetically favored due to their thermodynamically stable {101} facets. On the contrary, the HRTEM image of TNT-11 in Figure 1-3d prominently shows a lattice spacing of 0.238 nm corresponding to the (004) planes, whose facets are especially reactive in anatase TiO_2. The FFT patterns of TNT-2 and TNT-11 (the insets of Figure 1-3c and 3d, respectively) show squared spots, which can be indexed to the (101) and (004) planes. (004) diffraction is particularly strong in the FFT pattern of TNT-11, indicating that the nanocrystals of TNT-11 are preferentially aligned along the [001] direction, *i.e.* the (004) planes, of the anatase TiO_2 structure. Thus, based on our structural analyses, we can conclude that the high-reactive {001} facets are much more exposed in TNT-11 than in TNT-2.

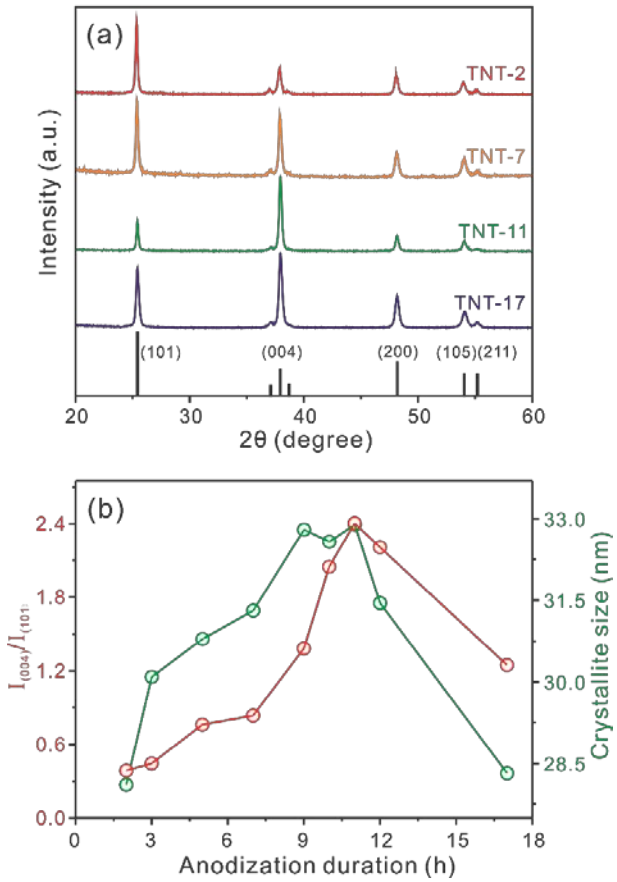

Figure 1-4. (a) HRXRD patterns of indicated TNT arrays. The standard diffraction pattern of anatase TiO_2 is also shown in the bottom. (b) (004)/(101) intensity ratios and crystallite sizes of TNT arrays versus the anodization duration.

All the diffraction peaks in the HRXRD patterns of Figure 1-4a correspond with well-known values of the pure anatase phase of TiO_2 (tetragonal, $I4_1/amd$, JCPDS 21-1272). The very sharp diffraction peaks of Figure 1-4a indicate that TNT arrays have good crystallographic structures. The further analysis of the peak broadening of crystal dimensions in the (004) peak at 2θ of 37.8° using the Scherrer's equation [33] has revealed the average crystallite sizes of 28.1,

31.3, 32.9, and 28.3 nm for the TNT-2, TNT-7, TNT-11, and TNT-17, respectively (Figure 1-4b and Table 1-S1). As illustrated in Figure 1-4b, the average crystallite size increases with the first anodization duration up to 11 h, indicating that TNT-11 has the best crystallinity among our prepared TNT arrays. Furthermore, Figure 1-4b also shows that the (004)/(101) intensity ratio of TNT arrays is highest when the first anodization duration is 11 h. Generally, the synergetic function of fluoride ions can markedly reduce the surface energy of the {001} facets to a level lower than that of the {101} facets [13]. The F-terminated surface, which stabilizes the (001) surfaces, could be maximized at the first anodization duration of 11 h. Figure 1-S3 and Table 1-S1reveal that the (004)/(101) intensity ratio of TNT arrays also increases with the concentration of NH_4F during the anodization of TNT-2 arrays. Taking the above observations into account, we can suggest that fluoride ions play a key role in the formation of TNT arrays dominated with the highly reactive the {001} facets. Based on our HRTEM and HRXRD analyses, TNT-11 arrays are considered to have the best crystal structure dominated with the highly energetic {001} facets.

To understand the surface composition of the product in detail, we have also measured high-resolution XPS spectra (Figure 1-S4 and S5). As illustrated in Figure 1-S4, the high-resolution XPS spectra of the F 1s region have been measured to probe F atoms existing on the surface of first-anodized TNT arrays. The high-resolution XPS spectra of the F 1s region show only one peak at 684.6 eV, a typical value for fluorinated TiO_2 such as surface Ti-F species that are

physically adsorbed on TiO_2 crystal surfaces [13]. Note that the F 1s peak at 688.6 eV, which is ascribed to the value of F atoms substituted for O atoms in the TiO_2 crystal lattice, is absent [34]. With the increase of the first-anodization time up to 11 h, the intensity of Ti–F species increases due to the adsorption of F^- ions onto passivated TiO_2 crystal facets. It is well-known that F^- ions stabilize the (001) surfaces significantly more than the (101) surfaces [35,36]. Therefore, Ti–F species are more abundant on the surfaces of TNT-11 than on the surfaces of other TNT arrays, leading to the more stabilization of the (001) surfaces and the relatively higher percentage of the exposed {001} facets on the surfaces of TNT-11. However, the surface Ti–F bonding is not favorable for photocatalysis because it can change five-coordinated Ti atoms in the exposed {001} facets into six-coordinated Ti atoms, which reduce the surface reactivity significantly [37]. Therefore, it is necessary to clean the surfaces via a simple heat treatment, which is sufficient enough without varying the crystal structure and morphology [37,38]. As shown in Figure 1-S4, calcined TNT-11 does not show any signal arising from F 1s electrons, indicating that the F atoms have been thoroughly removed from the surfaces of TNT-11. Furthermore, the XPS spectra of O 1s and Ti 2p for TNT-2 are very similar to the respective ones for TNT-11 (Figure 1-S5). Each O 1s spectrum of TNT-2 and TNT-11 has been deconvoluted into three peaks with binding energies of 529.9 (59%), 531.2 (10.2%), and 532.4 eV (2.8%). The first peak at 529.9 eV has been attributed to lattice oxygen atoms in stoichiometric TiO_2 while the second peak to non-lattice oxygen atoms in oxygen-deficient TiO_x ($x < 2$). Finally, the third one

around 532.4 eV has been assigned to oxygen atoms in surface species such as Ti-OH and adsorbed water molecules remained at the TiO_2 surface. On the other hand, the absence of O 1s peak at 534.0 eV, which is attributed to organic species as an impurity, indicates that TNT-2 and TNT-11 have clean surfaces. The right side of Figure 1-S5 shows that the binding energies of Ti $2p_{1/2}$ and $2p_{3/2}$ for both TNT-2 and TNT-11 are 464.3 and 458.6 eV, respectively, indicating that the oxidation state of the Ti element in our TNT arrays is the same as that of bulk TiO_2 [39].

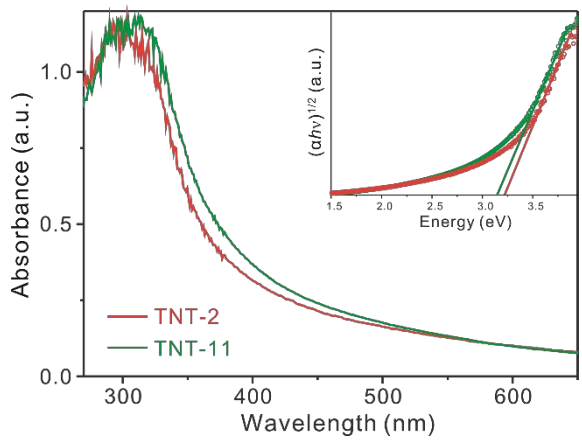

Figure 1-5. UV-visible absorption spectra of indicated TNT arrays suspended in water. The inset shows the $(\alpha h\nu)^{1/2}$ plots against energy ($h\nu$) of the absorption spectra, where α is the absorption coefficient and the solid lines show the best linear fits to estimate the band-gap energies.

Anatase TiO_2 crystals exposed with dissimilar crystal facets, which have their own unique arrangement of surface atoms, exhibit different electronic band structures [40]. Because the electronic band structure is one of the important factors that influence the photocatalytic activity, we have inferred

the electronic band gaps of TNT-2 and TNT-11 by UV-visible spectroscopy (Figure 1-5). It can be found that TNT-2 and TNT-11 have similar absorption spectra but that the absorption edge of TNT-11 is slightly red-shifted by 6 nm with respect to that of TNT-2. We have estimated the band-gap energies of TNT arrays, which are indirect band-gap materials, by extrapolating the linear portion of the modified Kubelka–Munk plot as shown in the inset of Figure 1-5 [18]; the band-gap energy of TNT-11 (3.16 eV) is slightly decreased by 0.05 eV from that of TNT-2 (3.21 eV). It has been reported that the {001} facet has a smaller band gap than the {101} facet due to different atomic configuration [18,40]. Thus, we suggest that the higher percentage of the {001} facets in TNT-11 is responsible for the decrease of the band-gap energy.

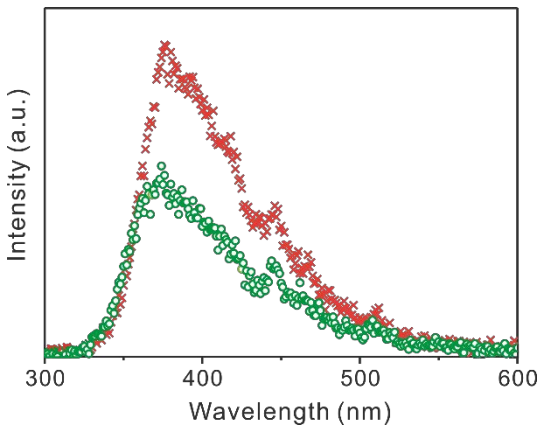

Figure 1-6. PL spectra of (red) TNT-2 and (green) TNT-11 in water with excitation at 280 nm.

PL spectra can be measured to understand the trapping, migration, and transfer of charge carriers in semiconductor particles because PL results from

the recombination of free carriers [16,18]. Figure 1-6 shows that the PL spectra of TNT-2 and TNT-11 are spectrally similar to each other as both samples have the anatase phase of TiO_2. The strong peak around 370 nm is ascribed to the band-gap transition whose energy is approximately equal to the band-gap energy of anatase TiO_2 (3.2 eV), and the shoulder peak around 440 nm is primarily attributed to self-trapped excitons and oxygen vacancies [41,42]. Oxygen vacancies have been considered as the most common defects and usually act as active centers in luminescence processes. Therefore, Figure 1-6 suggests that luminescent oxygen defects reside more intensively in TNT-2 than in TNT-11, indicating that compared with TNT-2, TNT-11 has the well-defined –Ti–O– network of anatase TiO_2 with a minimal amount of trap sites and oxygen vacancies to yield weaker PL intensity. Also, the intensity of defect PL in TNT arrays depends on carrier transport, which competes with radiative recombination, as well as the density of defects [43]. Our PL results of Figure 1-6 imply that the lower PL intensity of TNT-11 could have positive influence in the photocatalytic activity (see below) [16,42].

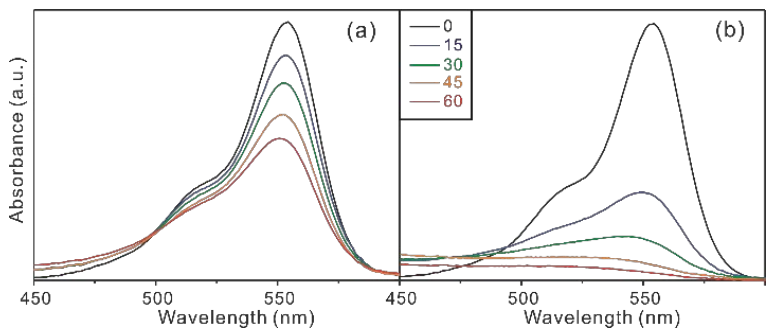

Figure 1-7. Photocatalytic absorption spectral changes of 10 μM RhB(aq) in the presence of (a) TNT-2 and (b) TNT-11 with elapsed times indicated in the units of min.

Generally, the performances of photocatalysts are significantly influenced by the coordination of surface atoms and the percentage of exposed reactive crystal facets. Thus, the photocatalytic activity of TNT arrays has been investigated by monitoring the time-dependent absorbance changes of RhB with TNT arrays under UV light irradiation. RhB, which is often used as a probe molecule to evaluate the photocatalytic performance, is a highly photostable pollutant organic dye. The photodegradation of RhB has been observed to be negligible in the absence of TNT arrays. Figure 1-7 indicates that TNT arrays have high photocatalytic performances; in particular, 98% of RhB has been decomposed within 1 h when TNT-11 has been present at a concentration of 0.17 g L^{-1}.

Figure 1-8a shows that the curves of $\ln(C/C_0)$ versus the degradation time, the photodegradation kinetic plots of RhB via TNT arrays, have linear relation for all the samples, indicating that the photocatalytic degradation of RhB follows pseudo first-order kinetics and that k, the photocatalytic degradation rate constant of RhB via TNT arrays, can be obtained from $\ln(C/C_0) = -kt$ [9]. The calculated k values of all the TNT arrays are summarized in Figure 1-8b and Table 1-S1. Figure 1-8b shows clearly that the photocatalytic activity of TNT arrays depends highly on the (004)/(101) intensity ratio of TNT arrays; TNT-11 with the largest fraction of the {001} facets has the best photocatalytic performance ($k = 0.062$ min^{-1}) whereas TNT-2 with the lowest fraction of the {001} facets shows the lowest photocatalytic performance ($k = 0.010$ min^{-1}). The photo-degradation kinetic data of phenol in Figure 1-S6 also indicate that

the photocatalytic activity of TNT-11 ($k = 0.0065\ min^{-1}$) is much higher than that of TNT-2 ($k = 0.0021\ min^{-1}$). Thus, Figure 1-8b, S6 and Table 1-S1 designate that the preparation of anatase TNT arrays dominated with highly energetic {001} facets is crucial for high photocatalytic performances. Also, as shown in Figure 1-S7 and Table 1-S1, the photocatalytic performances of TNT arrays with (004)/(101) intensity ratios controlled by varying the concentration of NH_4F indicate that the photocatalytic activity of TNT-2 (2.5%) with the highest exposed degree of the {001} facets is much more efficient than that of TNT-2 (0.5%) with the lowest exposed degree of the {001} facets. Thus, not only Figure 1-8 but also Figure 1-S7 indicate that the photocatalytic activity of TNT arrays increases with increase in the exposed degree of the {001} facets, suggesting that the highly energetic {001} facets enhance the photocatalytic activity of TNT arrays highly.

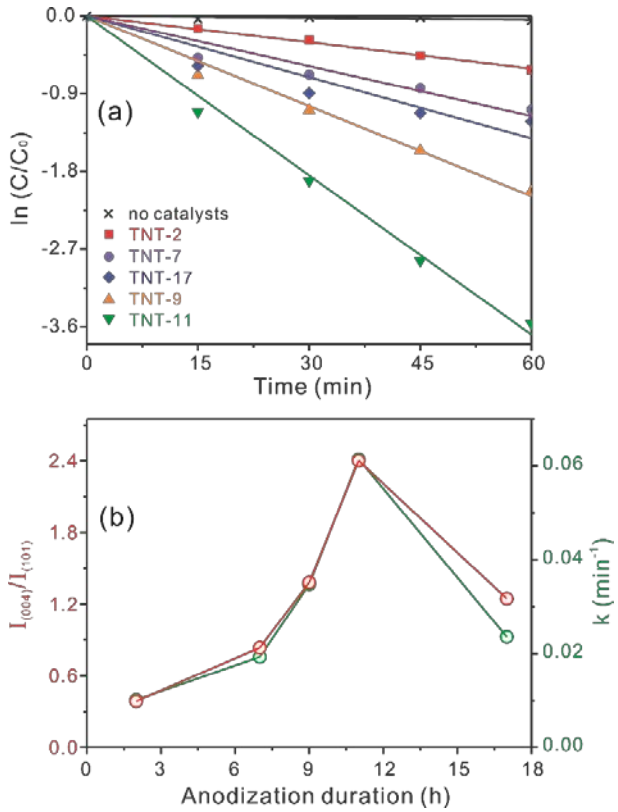

Figure 1-8. (a) First-order kinetics, ln (C/C_0) versus the irradiation time, for the photocatalytic degradation of 10 μM RhB(aq) via indicated TNT arrays. (b) (red) (004)/(101) intensity ratios and (green) photocatalytic rate constants as a function of the anodization duration.

In general, it is well known that the photocatalytic reaction of TiO_2 proceeds mainly by the contribution of active oxygen species such as H_2O_2, $\bullet O_2^-$, and •OH. The hydroxyl radical of •OH is a highly reactive oxidant so that its reaction ability is high enough to attack any organic substances [44,45]. Hence, we have also carried out photocatalytic experiments with excessive addition of sodium sulfite as a hole scavenge in Figure 1-S8 to examine the oxidation

reactivity of photogenerated holes. As an enough amount of sodium sulfite was added, the photocatalytic reaction did not take place in the beginning because all the photogenerated holes were scavenged by sulfite ions. However, the photocatalytic reaction occurred slowly with the increase of the time as holes were photogenerated continuously at a fixed concentration of sulfite ions. Figure 1-S8 indicates that at the same concentration of sodium sulfite the photocatalytic reaction of TNT-11 recovered more rapidly than that of TNT-2. It has been reported that the anatase {001} facet, as well as the rutile {011} facet, of TiO_2 provides oxidation sites extensively [46]. Thus, Figure 1-S8 also supports that compared TNT-2, TNT-11 has the improved photooxidation activity because TNT-11 has the higher exposed degree of the highly energetic {001} facets.

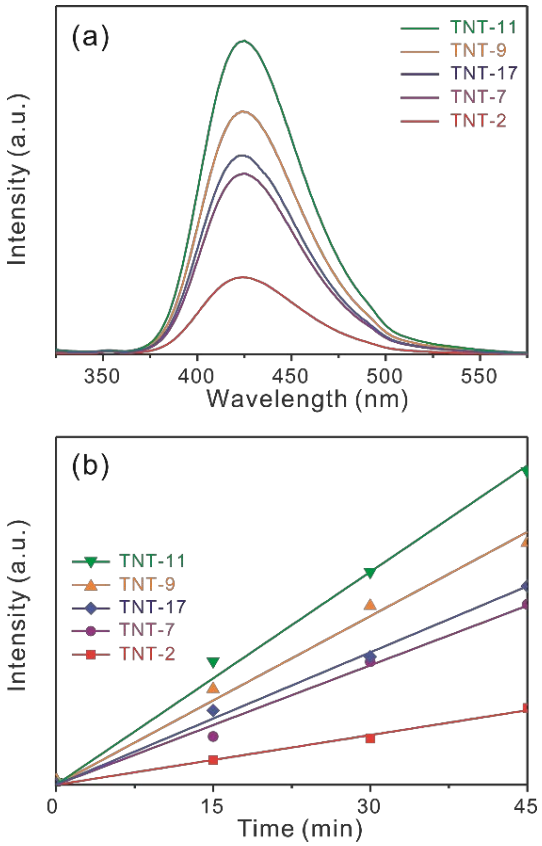

Figure 1-9. (a) PL spectra of TAOH generated with indicated TNT arrays for 45 min. (b) The fluorescence intensity at 425 nm of TAOH versus the irradiated time with indicated TNT arrays.

The nature of the photocatalytic performance has been further proved by measuring the formation of active •OH using terephthalic acid (TA) as a fluorescence probe under UV irradiation. The formation of •OH at illuminated catalysts has been detected by measuring fluorescence derived by the reaction with TA, which readily reacts with generated •OH to form a highly fluorescent product of 2-hydroxyterephthalic acid (TAOH) [28,29]. Figure 1-9a displays that the PL intensity of TAOH generated for 45 min with TNT-11 was higher

than that with any other TNT arrays; especially, the fluorescent intensity of TAOH with TNT-11 was 4 times higher than that with TNT-2. Thus, Figure 1-9a designates that the formation of •OH via TNT-11 was superior to that with any other TNT arrays. As shown in Figure 1-9b, the gradual formation intensity of •OH via TNT arrays was proportional to the irradiation time. On the whole, considering Figure 1-9 as well as Figure 1-8, we suggest that •OH is the predominant highly active species for the photocatalytic degradation of organic dye pollutants via TNT arrays [47].

1. 5. Conclusion

Well-defined uniform anatase TiO_2 nanotube (TNT) arrays with the predominant exposure of the highly energetic {001} facets have been successfully prepared via a two-step anodic oxidation process of Ti foil. In order to enhance the exposure degree of the {001} facets, NH_4F has been used as a fluorine source for an excellent crystallography-controlling capping agent during anodization; fluoride ions markedly reduce the surface energy of the {001} facets. The evolution of TNT arrays has been varied by changing the duration of anodization and the concentration of NH_4F. With the increase of the first-anodization time (up to 11 h) and/or the NH_4F concentration, the photocatalytic activity, as well as the crystallite sizes, crystallinity, and exposed {001} facets, of prepared TNT arrays has been found to increase. In particular, the photocatalytic activity of TNT arrays increases in accordance with increase in the exposure degree of the {001} facets, suggesting that the highly energetic {001} facets enhance the photocatalytic activity of TNT arrays on a large scale. Our diverse characterization results have shown that the {001} facets of TNT arrays provide oxidation sites extensively, which produce active oxygen species such as •OH, $\bullet O_2^-$, and H_2O_2 upon UV irradiation. We have also shown clearly that •OH is the predominant highly active species for the photocatalytic degradation of organic dye pollutants via TNT arrays. Thus, we consider that this study may provide a new insight into the preparation and development of advanced photocatalytic anatase TiO_2 materials.

1. 6. Acknowledgement

This work was supported by research grants through the National Research Foundation of Korea funded by the Korea government (2014-057382 and 2015-051798).

1. 7. Supporting information

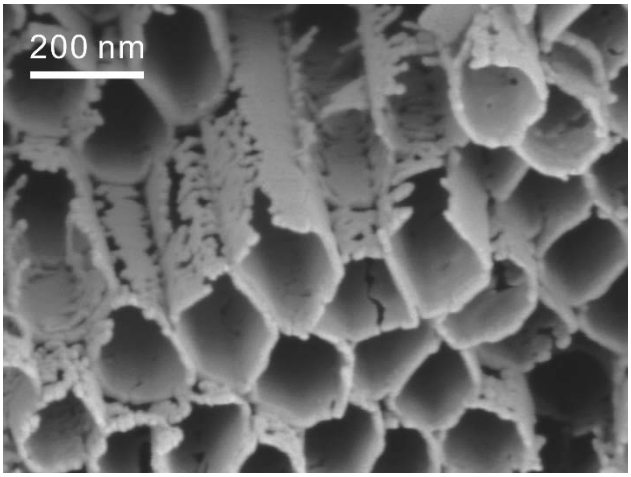

Figure 1-S1. FESEM image of collapsed TNT-17.

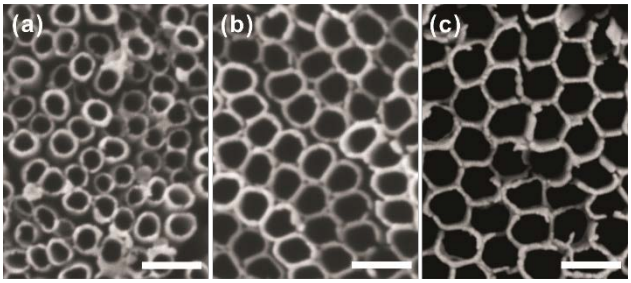

Figure 1-S2. FESEM images of (a) TNT-2 (0.5%), (b) TNT-2 (1.0%), and (c) TNT-2 (2.5%). Each scale bar indicates 200 nm.

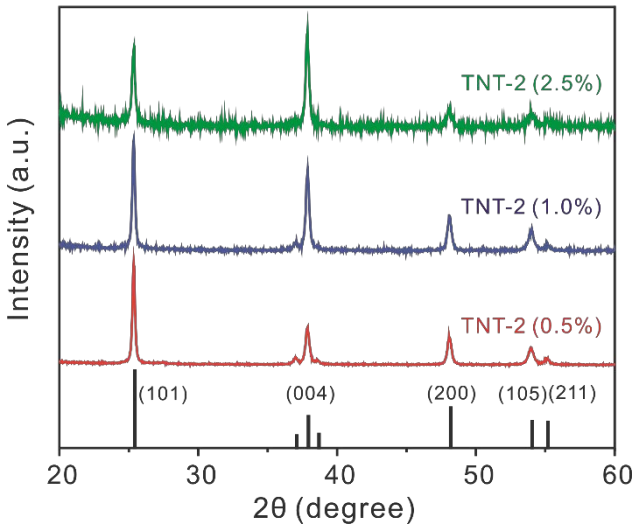

Figure 1-S3. HRXRD patterns of indicated TNT arrays. The standard diffraction pattern of anatase TiO_2 is also shown in the bottom.

Table 1-S1. Average crystallite sizes (d), (004)/(101) intensity ratios (R), and rate constants (k) for the catalytic degradation of 10 μM RhB(aq) via TNT arrays under irradiation by a 300 W Xe lamp.

	[NH_4F] (%)	time (h)	d (nm)	R	k (min^{-1}) [a]
TNT-2	0.5	2	28.1	0.39 (18%)[b]	0.010
TNT-7	0.5	7	31.3	0.75 (24%)	0.019
TNT-9	0.5	9	32.8	1.38 (41%)	0.035
TNT-11	0.5	11	32.9	1.79 (52%)	0.062
TNT-17	0.5	17	28.3	1.27 (36%)	0.026
TNT-2 (1.0%)	1.0	2	30.5	0.69 (28%)	0.013
TNT-2 (2.5%)	2.5	2	31.9	1.14 (34%)	0.024

[a] The photodegradation rate constant in the absence of TNT arrays is 0.0007 min^{-1}. [b] The specific percentage of {001} facets calculated by dividing the count of the (004) peak by the total count of a HRXRD pattern.

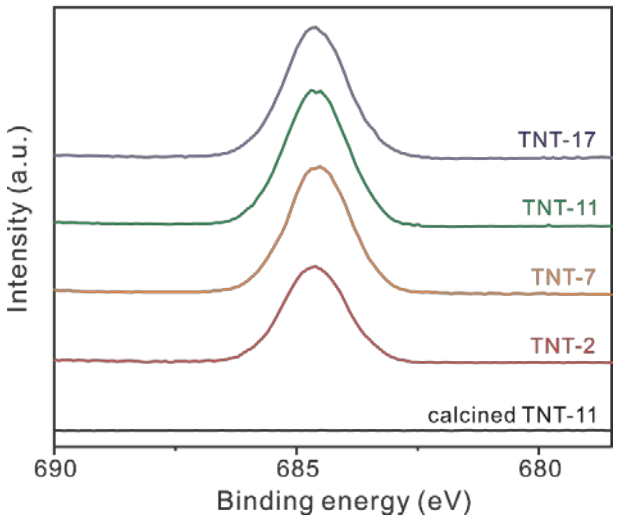

Figure 1-S4. High-resolution XPS spectra of F 1s for indicated first-anodized TNT arrays and calcined TNT-11.

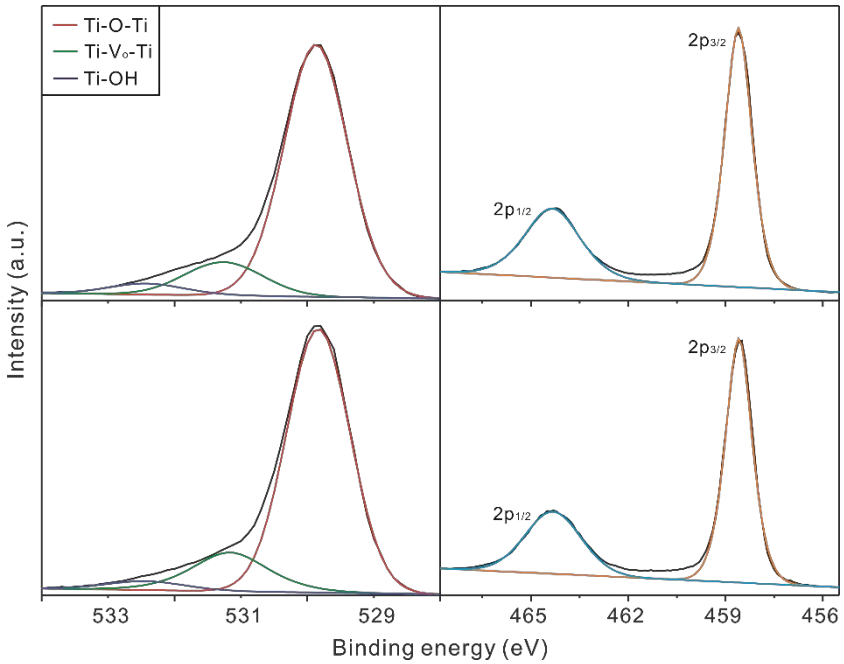

Figure 1-S5. High-resolution XPS spectra of (left) O 1s and (right) Ti 2p for (top) TNT-2 and (bottom) TNT-11.

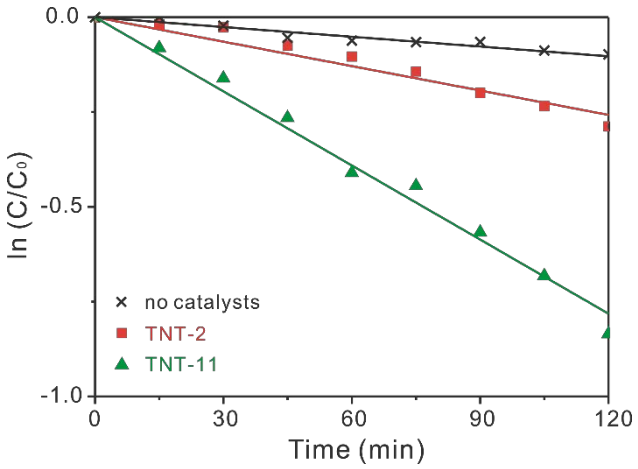

Figure 1-S6 First-order kinetics, ln (C/C_0) versus the irradiation time, of phenol(aq) degradation in the presence of indicated TNT arrays.

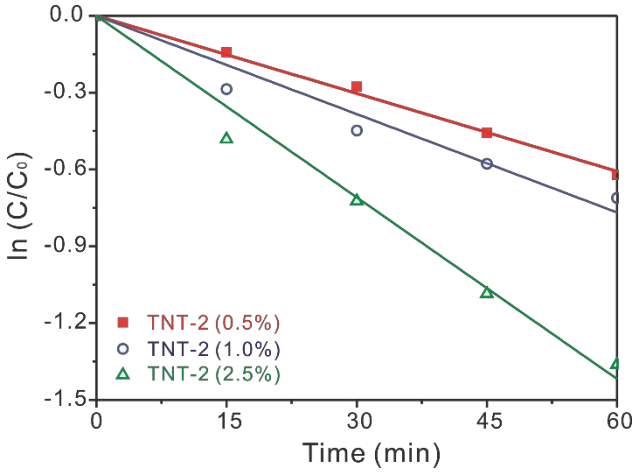

Figure 1-S7. First-order kinetic plots for the photocatalytic degradation of 10 μM RhB(aq) in the presence of indicated TNT arrays.

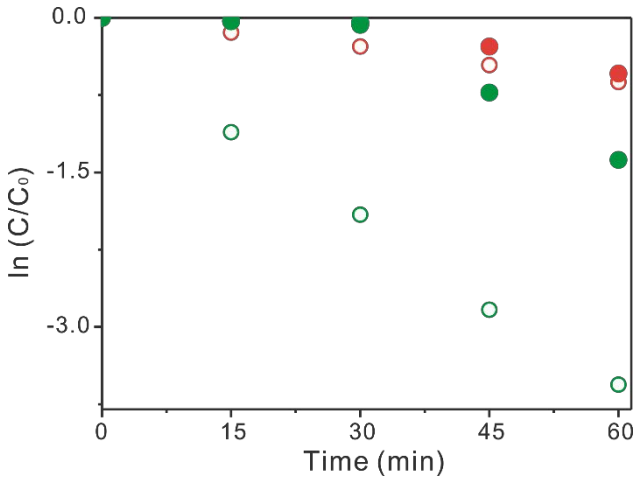

Figure 1-S8. First-order kinetics, ln (C/C_0) versus the irradiation time, of RhB(aq) degradation via (red) TNT-2 and (green) TNT-11 in (open) the absence and (closed) the presence of sodium sulfite.

1. 8. References

[1] D. Gust, T.A. Moore, A.L. Moore, Acc. Chem. Res. 42 (2009) 1890-1898.

[2] J.R. Bolton, Solar fuels, Science 202 (1978) 705-711.

[3] H. Wang, L. Zhang, Z. Chen, J. Hu, S. Li, Z. Wang, J. Liu, X. Wang, Chem. Soc. Rev. 43 (2014) 5234-5244.

[4] T. Hisatomi, J. Kubota, K. Domen, Chem. Soc. Rev. 43 (2014) 7520-7535.

[5] J. Schneider, M. Matsuoka, M. Takeuchi, J. Zhang, Y. Horiuchi, M. Anpo, D.W. Bahnemann, Chem. Rev. 114 (2014) 9919-9986.

[6] X. Chen, S. Shen, L. Guo, S.S. Mao, Chem. Rev. 110 (2010) 6503-6570.

[7] M.-C. Yang, Y.-Y. Lee, B. Xu, K. Powers, Y.S. Meng, J. Power Sources 207 (2012) 166-172.

[8] J. Bai, B. Zhou, Chem. Rev. 114 (2014) 10131-10176.

[9] J.-Y. Kim, D. Lee, H.J. Kim, I. Lim, W.I. Lee, D.-J. Jang, J. Mater. Chem. A 1 (2013) 5982-5988.

[10] G. Liu, H.G. Yang, J. Pan, Y.Q. Yang, G.Q. Lu, H.M. Cheng, Chem. Rev. 114 (2014) 9559-9612.

[11] W.Q. Fang, X.-Q. Gong, H.G. Yang, J. Phys. Chem. Lett. 2 (2011) 725-734.

[12] W.J. Ong, L.L. Tan, S.P. Chai, S.T. Yong, A.R. Mohamed, Nanoscale 6 (2014) 1946-2008.

[13] H.G. Yang, C.H. Sun, S.Z. Qiao, J. Zou, G. Liu, S.C. Smith, H.M. Cheng, G.Q. Lu, Nature 453 (2008) 638-641.

[14] S. Liu, J. Yu, M. Jaroniec, Chem. Mater. 23 (2011) 4085-4093.

[15] Z. Wang, K. Lv, G. Wang, K. Deng, D. Tang, Appl. Catal. B 100 (2010) 378-385.

[16] Q. Xiang, K. Lv, J. Yu, Appl. Catal. B 96 (2010) 557-564.

[17] X.H. Yang, Z. Li, C. Sun, H.G. Yang, C. Li, Chem. Mater. 23 (2011) 3486-3494.

[18] H.-B. Kim, H. Kim, W.I. Lee, D.-J. Jang, J. Mater. Chem. A 3 (2015) 9714-9721.

[19] K. Lv, B. Cheng, J. Yu, G. Liu, Phys. Chem. Chem. Phys. 14 (2012) 5349-5362.

[20] M. Cargnello, T.R. Gordon, C.B. Murray, Che. Rev. 114 (2014) 9319-9345.

[21] C. Xiong, X. Deng, J. Li, Appl. Catal. B 94 (2010) 234-240.

[22] A.-I. Zhang, L.-L. Long, C. Liu, W.-W. Li and H.-Q. Yu, Green Chem., 16 (2014) 2745-2753.

[23] M.Y. Hsu, H.L. Hsu, J. Leu, J. Electrochem. Soc. 159 (2012) H722-H727.

[24] N. Rausch, E. Burte, J. Electrochem. Soc. 140 (1993) 145-149.

[25] R.A. Caruso, J.H. Schattka, A. Greiner, Adv. Mater. 13 (2001) 1577-1579.

[26] J. Tao, J. Zhao, C. Tang, Y. Kang, Y. Li, New J. Chem. 32 (2008) 2164-2168.

[27] Ghicov, P. Schmuki, Chem. Commun. (2009) 2791-2808.

[28] J.C. Barreto, G.S. Smith, N.H. Strobel, P.A. McQuillin, T.A. Miller, Life Sci. 56 (1994) PL89-PL96.

[29] H. Lin, L. Li, M. Zhao, X. Huang, X. Chen, G. Li, R. Yu, J. Am. Chem. Soc. 134 (2012) 8328-8331.

[30] D. Lee, H.-B. Kim, S. Yu, H.J. Kim, W.I. Lee, D.-J. Jang, J. Mater. Sci. 49 (2014) 3414-3422.

[31] J.M. Macak, S. Albu, D.H. Kim, I. Paramasivam, S. Aldabergerova, P. Schmuki, Electrochem. Solid-State Lett. 10 (2007) K28-K31.

[32] U. Diebold, Surf. Sci. Rep. 48 (2003) 53-229.

[33] B. Karunagaran, R. Rajendra Kumar, D. Mangalaraj, S.K. Narayandass, G. Mohan Rao, Cryst. Res. Technol. 37 (2002) 1285-1292.

[34] Z. Zheng, B. Huang, J. Lu, X. Qin, X. Zhang, Y. Dai, Chem. Eur. J. 17 (2011) 15032-15038.

[35] X. Ma, Y. Dai, W. Wei, B. Huang, and M.-H. Whangbo, J. Phys. Chem. Lett. 6 (2015) 1876-1882.

[36] X. Ma, Y. Dai, M. Guo, and B. Huang, J. Phys. Chem. C 117 (2013) 24496−24502.

[37] Y. Liao, H. Zhang, W. Que, P. Zhong, F. Bai, Z. Zhong, Q. Wen, W. Chen, ACS Appl. Mater. Interfaces. 5 (2013) 6463-6466.

[38] X. Wu, Z. Chen, G.Q.M. Lu, L. Wang, Adv. Funct. Mater. 21 (2011) 4167-4172.

[39] P. Georgios, S.M. Wolfgang, Solid State Phenom. 162 (2010) 163-177.

[40] G. Liu, C. Sun, H.G. Yang, S.C. Smith, L. Wang, G.Q. Lu, H.M. Cheng, Chem. Commun. 46 (2010) 755-757.

[41] B. Santara, P.K. Giri, K. Imakita, M. Fujii, Nanoscale 5 (2013) 5476-5488.

[42] R.G. Nair, S. Paul, S.K. Samdarshi, Sol. Energy Mater. Sol. Cells 95 (2011) 1901-1907.

[43] C. Mercado, Z. Seeley, A. Bandyopadhyay, S. Bose, J.L. McHale, ACS Appl. Mater. Interfaces 3 (2011) 2281-2288.

[44] Haarstrick, O.M. Kut, E. Heinzle, Environ. Sci. Technol. 30 (1996) 817-824.

[45] M.J. Berr, A. Vaneski, C. Mauser, S. Fischbach, A.S. Susha, A.L. Rogach, F. Jackel, J. Feldmann, Small 8 (2012) 291-297.

[46] M. D'Arienzo, J. Carbajo, A. Bahamonde, M. Crippa, S. Polizzi, R. Scotti, L. Wahba, F. Morazzoni, J Am Chem Soc, 133 (2011) 17652-17661.

[47] H.G. Yang, G. Liu, S.Z. Qiao, C.H. Sun, Y.G. Jin, S.C. Smith, J. Zou, H.M. Cheng, G.Q. Lu, J. Am. Chem. Soc. 131 (2009) 4078-4083.

Chapter 2. Morphology evolution of Ag/Au nanocomposites via temperature-controlled galvanic exchange to enhance catalytic activity

2. 1. Abstract

Morphology-controlled Ag/Au nanocomposite have been fabricated facilely via a modified galvanic replacement reaction using Ag nanocubes as sacrificial templates. The structures of Ag/Au nanocomposites produced at the galvanic reaction temperatures of 0, 25, 55, 85, and 105 ^{o}C have been found as Au-decorated Ag nanocubes, well-defined nanoboxes, truncated nanoboxes, and porous nanoboxes, and broken nanoboxes, respectively. Compared to pristine Ag nanocubes or Ag/Au nanocomposites without cavities, Ag/Au nanocatalysts with hollow interiors have been found to catalyze the degradation of rhodamine B more rapidly in the presence of KBH_4. In particular, Ag/Au nanocomposites fabricated at 85 ^{o}C show the most efficient catalytic performances as their largest nanocavities are surrounded by the most porous walls. The high enhancement of catalytic performances is attributed to the facilitation of rapid electron relays from BH_4^- to rhodamine B through the catalytic surface, lowering the kinetic barrier of the catalytic reaction consequently. Overall, the temperatures of galvanic replacement reactions have been varied to optimize the morphologies and the subsequent catalytic performances of Ag/Au nanocomposites.

2. 2. Introduction

Metallic nanostructured materials have received a great deal of research effort owing to their outstanding physical and chemical properties depending on sizes, shapes, and compositions [1-3]. In particular, there has been a growing interest in nanostructures comprising noble metals due to their unusual physicochemical characteristics which are considerably different from the respective properties of bulk-sized ones [4,5]. In this respect, the fabrication of nanometer-sized noble metals has led to intrigue applications in various associated fields such as photography, spectroscopy, optoelectronics, sensing, biological labeling, and catalysis [6-8]. Bimetallic nanostructures consisting of noble metals such as gold, palladium, platinum, and silver have received special attention because their unique optical, electronic, and catalytic properties lead to a broad range of applications, including localized surface-plasmon resonance, surface-enhanced Raman scattering, biosensor, and catalysis [9,10]. For example, by combining Ag and Au into a single entity, catalytic properties can be further improved and localized surface-plasmon adsorption can be varied continuously to the limits of corresponding monometallic particles [11,12]. Diverse approaches to synthesize the bimetallic nanomaterials have been investigated: the simultaneous chemical reduction of mixed metal ions, the electrochemical reduction, and the successive reduction of metal ions on the surface of sacrificial nanoparticles, which is known as the galvanic replacement reaction [13,14].

The galvanic replacement reaction is basically a redox process between two metals

with distinct reduction potentials. The oxidation takes place in one metal with a low reduction potential which is referred to as a sacrificial template, and the reduction coincides with the deposition on the other metal with a high reduction potential [15-17]. This simple process is controlled solely by a favorable difference between the reduction potentials of two metals. The galvanic replacement provides a simple and versatile route to engineering a range of advance multifunctional nanostructures such as hollow interiors and porous walls [14,18,19]. Among various noble metal-based nanostructures, hollow architectures are a particularly interesting class of materials that have unusual chemical and physical properties compared to the respective ones of solid counterparts [20-22]. The galvanic replacement process has been employed as a useful method for preparing hollow metallic composite nanostructures including spherical nanoshells, nanodendrites, nanoboxes, nanocages, nanotubes, and nanoframes consisting of Au, Pd, and/or Pt by using Ag, Cu, or more reactive metals as sacrificial templates [23-25]. These hollow metallic composite nanostructures have a great deal of promise for diverse fields including photothermal therapy, biomedical imaging, drug delivery, and electrochemical catalysis. In particular, catalytic performances can be optimized by controlling surface compositions, sizes, and morphologies carefully [14,25,26]. Hollow-structured Ag/Au nanocomposites exhibit high catalytic activity as they have high surface-to-volume ratios, low densities, and two different types of surfaces, which are the interior and the exterior walls of hollow nanostructures.

Herein, we have controlled the morphologies of Ag/Au nanocomposites via modified galvanic replacement reactions involving Ag nanocubes as sacrificial

templates; the variation of reaction temperatures has resulted in the nanostructure modification of Ag/Au nanocomposites. Whereas Ag/Au nanocomposites prepared at 25 and 55 °C look like nanoboxes and truncated nanoboxes, respectively, Ag/Au nanocomposites fabricated at 85 °C resemble porous nanoboxes, as shown in Figure 2-1. We have compared the catalytic activity of Ag/Au nanocomposites prepared at various reaction temperatures by monitoring the catalytic degradation rate constants and other kinetic parameters of rhodamine B (RhB) in the presence of BH_4^-. It has been found that the catalytic rate constant via Ag/Au nanocomposites prepared at 85 °C is higher by factors of 2.2, 1.5, and 100 than the rate constants of Ag/Au nanocomposites prepared at 25, 55, and 105 °C, respectively. This indicates that we can control the morphologies of Ag/Au nanocomposites to enhance their catalytic performances readily by adjusting the temperatures of galvanic replacement reactions.

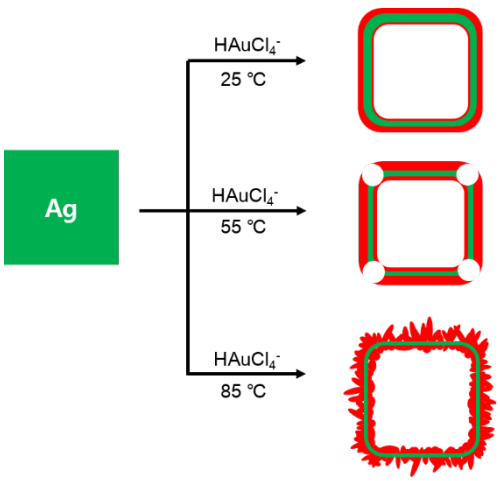

Figure 2-1. Illustration for the temperature-controlled morphology evolution of Ag/Au nanocomposites.

2. 3. Experimental section

2.1. Materials

Chemicals were used as purchased without further purification: CF_3COOAg (s, ≥99.9%), $HAuCl_4 \cdot 3H_2O$ (s, ≥99.9%), polyvinylpyrrolidone (PVP, s, Mw = 55,000), $Na_2S \cdot 9H_2O$ (s, ≥99.9%), 37% HCl(aq), and KBH_4 (s, ≥95%) from Sigma-Aldrich; ethylene glycol (EG, ℓ, 99%) from Daejung Chemicals; rhodamine B (RhB, s) from Wako Chemicals. Deionized water (>15 MΩ cm) from an Elga PURELAB Option-S system was used throughout the experiments.

2.2. Synthesis of Ag nanocubes

Pristine Ag nanocubes (Ag_{pr}) were synthesized via a sulfide-mediated polyol process, with EG as the solvent and CF_3COOAg as a precursor of elemental silver [21,22,27]. In a typical synthesis, 20 mL of EG was added into a 100 mL round-bottom flask and heated in an oil bath at 160 °C for 30 min under magnetic stirring to remove residual water. 0.24 mL of 3.0 mM $Na_2S \cdot 9H_2O$(EG) was then injected quickly into the preheated EG. After 2 min, 2.0 mL of 3.0 mM HCl(EG) and 5.0 mL of 20 mg mL^{-1} PVP(EG) were quickly injected into the mixture. After additional 2 min, 1.6 mL of 282 mM CF_3COOAg(EG) was added into the mixture, which was then reacted for 20 min at 160 °C. During the entire reaction, the flask was capped with a rubber stopper except for the injection of reagents. The reaction mixture was quenched by placing the flask in an ice-water bath and added with acetone. The produced colloid was centrifuged, rinsed with acetone and three times with water to remove remaining

EG and PVP, and re-dispersed in water, yielding an aqueous colloidal solution of Ag_{pr}.

2.3. Preparation of Ag/Au nanocomposites

Ag/Au nanocomposites were prepared via galvanic replacement reactions between Ag_{pr} and $HAuCl_4$ in water. 0.30 mL of the Ag_{pr} colloid was dispersed in 5.0 mL of 1.0 mg mL^{-1} PVP(aq) and heated to a specific reaction temperature. 1.0 mL of 0.50 mM $HAuCl_4$(aq) was then added into the mixture, which was maintained for 20 min at the temperature. Then, the produced Ag/Au nanocomposites were centrifuged, rinsed with water three times, and then dispersed in water. To adjust the morphology of Ag/Au nanocomposites, the temperatures of galvanic replacement reactions were varied from 0 to 105 ^oC; hereafter, Ag/Au nanocomposites prepared at 0, 25, 55, 85, and 105 ^oC will be described as Ag/Au_0, Ag/Au_{25}, Ag/Au_{55}, Ag/Au_{85}, and Ag/Au_{105}, respectively.

2.4. Characterization

Whereas transmission electron microscopy (TEM) images were taken with a Hitachi H-7600 microscope, scanning transmission electron microscopy (STEM) images and energy-dispersive X-ray (EDX) elemental profiles and maps were measured with a JEOL JEM-2100F microscope. UV−visible absorption spectra were recorded by using a Scinco S-3000 spectrophotometer.

2.5. Measurement of catalytic properties

The catalytic performances of Ag/Au nanocomposites were measured by monitoring the degradation reaction of RhB in the presence of BH_4^-. 0.10 mL of a

nanocatalyst solution was added to 0.90 mL of water and 1.7 mL of 20 μM RhB(aq) contained in a quartz cuvette having a path length of 10 mm. The absorption changes of RhB(aq) were confirmed by using the above described temperature-controllable spectrophotometer at scheduled intervals after addition of 0.40 mL of 10 mM KBH_4(aq). Note that the concentrations of Ag and Au, calculated based on the respective precursor amounts, in a cuvette of catalysis experiments were 20 and 8.1 nM, respectively.

2. 4. Results and discussion

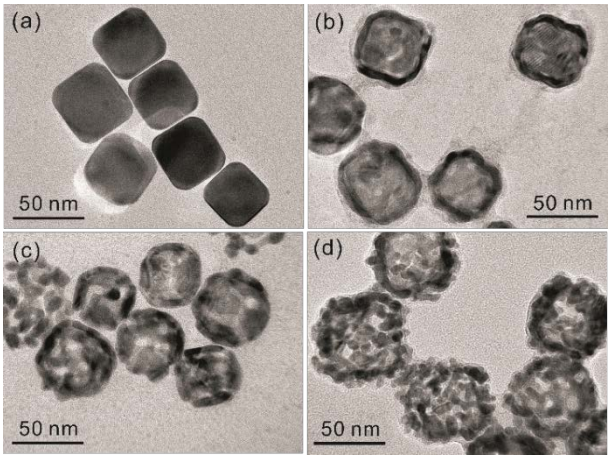

Figure 2-2. TEM images of (a) Ag_{pr}, (b) Ag/Au_{25} (c) Ag/Au_{55}, and (d) Ag/Au_{85}.

Figures 2-2 and S1 indicate that the evolution of different morphologies of Ag/Au nanocomposites has been induced by varying the temperatures of Ag templates-engaged galvanic replacement reactions. Well-defined nanocubes of Ag_{pr} (Figure 2-2a) with an average edge length of 43.1 ± 5.1 nm (Figure 2-S2a) were prepared for sacrificial nanotemplates via a typical sulfide-mediated polyol procedure [21,22,27]. As Ag_{pr} was mixed with $HAuCl_4$(aq), the galvanic replacement reaction took place immediately at the sites of the highest surface energy including defects, steps, or stacking faults [18]. Thus, Ag atoms were oxidized to dissolve into the aqueous solution, producing small holes on the surfaces of nanocubes. Concurrently, Au ions were reduced to become Au atoms. Since Ag and Au have the same face-centered cubic structure and similar lattice constants, Au atoms are prone to be epitaxially deposited on Ag surfaces, forming an incomplete thin layer [17,18]. Small holes

formed in the Au layer act as primary sites for the continuous dissolution of Ag. As a result, Ag_{pr} templates were partially dissolved to produce a cavity inside each nanoparticle. The temperature at which the galvanic replacement reaction takes place plays an important role in the formation of Ag/Au nanocomposites since the rate of the galvanic replacement reaction increases exponentially with temperature. Figure 2-S2 shows that the observed mean edge lengths of Ag/Au_0, Ag/Au_{25}, Ag/Au_{55}, Ag/Au_{85}, and Ag/Au_{105} are 48.7±10.8, 46.6±4.8, 46.9±5.3, 49.8±7.2, and 47.5±7.1 nm, respectively, supporting that reduced Au atoms have been deposited on the exterior surfaces of Ag nanotemplates. Figures 2-2 and S1 indicate that the structures of Ag/Au_0, Ag/Au_{25}, Ag/Au_{55}, Ag/Au_{85}, and Ag/Au_{105} are Au-decorated Ag nanocubes, well-defined nanoboxes, truncated nanoboxes, and porous nanoboxes, and amorphous nanocomposites, respectively. The hollow interiors of Ag/Au nanocomposites have been found in Ag/Au_{25}, Ag/Au_{55}, and Ag/Au_{85}; the average cavity sizes of Ag/Au_{25}, Ag/Au_{55}, and Ag/Au_{85} have been estimated as 29.8. 33.4, and 39.3 nm, respectively. The roughness and porosity of nanoboxes also increase with the increase of the reaction temperature. Thus, nanoboxes of Ag/Au_{85} have the largest cavities surrounded by the roughest and the most porous walls among our prepared Ag/Au nanocomposites. Note that nanobox structures having hollow interiors were not formed when the temperature was too low as 0 ^oC or too high as 105 ^oC. Overall, Figures 2-2, S1, and S2 indicate the morphologies of Ag/Au nanocomposites have been controlled facilely by adjusting the temperatures of galvanic replacement reactions.

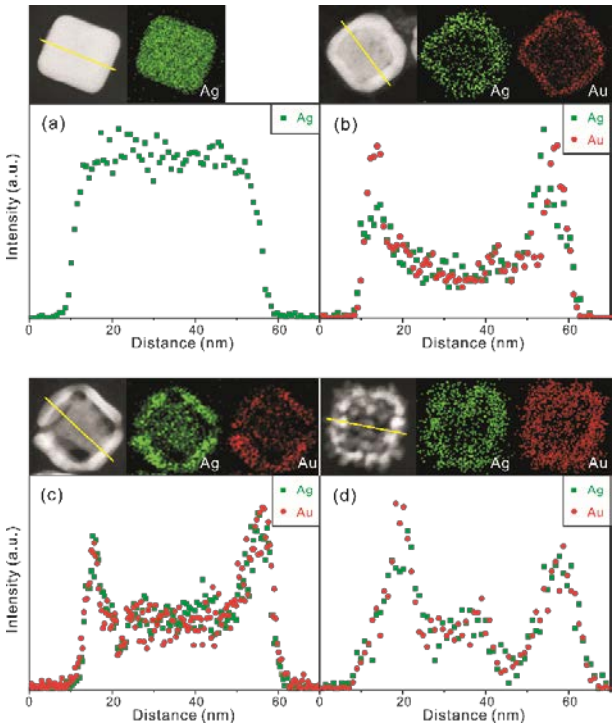

Figure 2-3. STEM images, EDX elemental maps, and area-normalized line-scanned elemental intensity profiles of (a) Ag_{pr}, (b) Ag/Au_{25}, (c) Ag/Au_{55}, and (d) Ag/Au_{85}.

The EDX line-scanned elemental profiles have been explored to confirm the elemental distributions and exact structures of Ag/Au nanocomposites. Figure 2-3a reveals that Ag_{pr} is a solid Ag nanocube with an edge size of 45.3 nm. Meanwhile, the line-scanned EDX elemental profiles of Ag/Au_{25} (Figure 2-3b), Ag/Au_{55} (Figure 2-3c), and Ag/Au_{85} (Figure 2-3d) show that two characteristic sharp peaks of Au are similar to the respective ones of Ag, indicating that the walls of a nanobox compositely consist of Ag and Au. A careful examination of the elemental profiles exhibits that the Ag edge sizes of Ag/Au_0 (Figure 2-S3), Ag/Au_{25}, Ag/Au_{55}, and Ag/Au_{85} are 31.2, 48.5, 45.8, and 49.1 nm, respectively, whereas the Au edge sizes of

Ag/Au_0, Ag/Au_{25}, Ag/Au_{55}, and Ag/Au_{85} are 47.1, 50.1, 46.1, and 49.2 nm, respectively. Thus, the Au edge size is larger than the Ag edge size in each examined Ag/Au nanocomposite, indicating that reduced Au atoms deposit on the exterior surfaces of Ag nanotemplates preferentially. As the reaction temperature increases, the mobility of atoms can be promoted rapidly by heat so that atomic exchange between Ag cores and Au shells takes place rapidly to form Ag/Au nanoalloys gradually. The STEM images and EDX elemental maps of Figures 2-3 and S3 also support that Ag/Au_0, Ag/Au_{25}, Ag/Au_{55}, and Ag/Au_{85} have nanostructures of Au-decorated Ag nanocubes, well-defined nanoboxes, truncated nanoboxes, and porous nanoboxes.

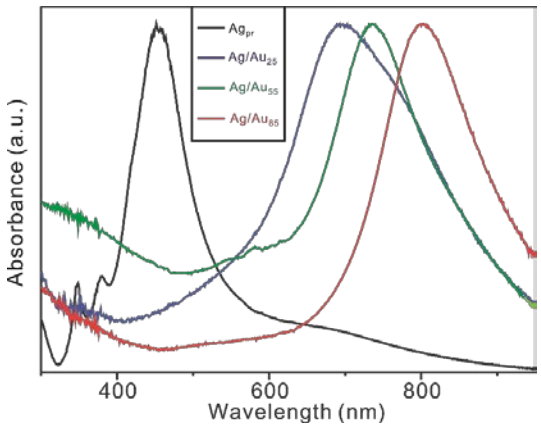

Figure 2-4. Maximum-normalized surface-plasmon resonance spectra of indicated nanocatalysts in water.

Variation in the surface-plasmon resonance (SPR) spectra of Ag_{pr}. Ag/Au_{25}, Ag/Au_{55}, and Ag/Au_{85} depicted in Figure 2-4 agrees well with the variation of morphologies, sizes, and compositions observed Figures 2-2 and 3. The SPR spectrum of Ag_{pr} shows three characteristic peaks of Ag nanocubes with an average

edge size of 43.1±5.1 nm, including the major SPR peak at 456±33 nm. Meanwhile, the SPR spectra of Ag/Au_{25}, Ag/Au_{55}, and Ag/Au_{85} have the absorption maxima at 693±102, 735±62, and 802±77 nm, respectively, indicating that the average length-to-thickness value for the walls of Ag/Au nanoboxes increases with the increase of the reaction temperature [28-30]. As shown in Figures 2-S1, S2, and S3, the SPR spectra of Figure 2-S4 also suggest that Au nanoplates and elliptical nanoparticles have been deposited on the surfaces of Ag nanotemplates for Ag/Au_0 while Ag/Au broken nanoboxes consisting of numerous thin nanoplates and nanodiscs with diverse sizes have been produced for Ag/Au_{105}.

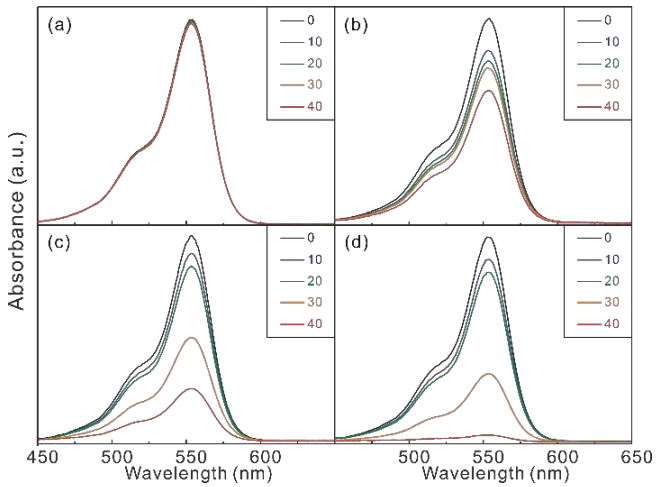

Figure 2-5. Absorption spectra at 25 °C of 11 μM RhB(aq) in the presence of 1.3 mM KBH_4, measured at times indicated in the units of min after addition of (a) Ag_{pr}, (b) Ag/Au_{25}, (c) Ag/Au_{55}, and (d) Ag/Au_{85}.

The catalytic performances of Ag/Au nanocomposites have been evaluated by monitoring the time-dependent absorption spectra of RhB degraded catalytically via as-prepared Ag/Au nanocomposites in the presence of BH_4^- as shown in Figures 2-5

and S5, indicating that the catalytic activity of Ag/Au nanocomposites depends highly on their morphologies [26,30,31], which have been varied by adjusting the temperature of the galvanic replacement reaction. RhB, which consists of a central xanthene ring connected to four N-ethyl groups, two on each side, exhibits high resistance to photodegradation [32,33]. Thus, the rapid degradation of RhB is important in regard to the purification of dye effluents. The residual concentration of RhB decomposed catalytically via Ag/Au nanocomposites in the presence of KBH_4 at a specific time has been estimated by monitoring the optical density of RhB at 554 nm. Figures 2-5 and S5 show that Ag/Au nanocomposites have much higher catalytic activities than Ag_{pr}; whereas only 2% has been decomposed in 40 min in the presence of Ag_{pr}, 70%, 35%, 49%, 97%, and 9% of RhB have been decomposed within 40 min in the presence of Ag/Au_0, Ag/Au_{25}, Ag/Au_{55}, Ag/Au_{85}, and Ag/Au_{105}, respectively. This also indicates that the catalytic activity is dependent strongly on the structures of Ag/Au nanocomposites. In particular, Ag/Au_{85} having the largest cavities surrounded by the most porous walls has shown the most efficient catalytic performance.

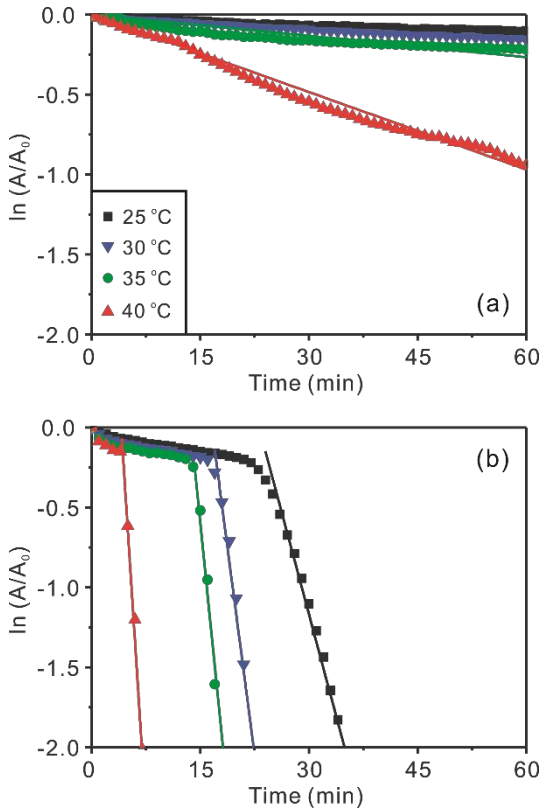

Figure 2-6. ln (A/A_0) vs t for the catalytic degradation of 11 μM RhB(aq) via (a) Ag_{pr} (b) Ag/Au_{85} in the presence of 1.3 mM KBH_4 at indicated temperatures.

Figure 2-6 shows that the time-dependent pseudo-first-order degradation profiles of RhB catalyzed by Ag_{pr} and $AgAu_{85}$ in the presence of KBH_4 have been used to elicit observed degradation rate constants (k_{obs}); the plots of $\ln (A/A_0) = -k_{obs} t$ [20,33], where A and A_0 are the optical densities of RhB at 554 nm at times t and 0, respectively, have been used to extract k_{obs} presented in Table 2-1. The catalytic rate constant of a Ag/Au nanocatalyst (k) has been extracted by subtracting the degradation rate constant of RhB in the absence of any nanocatalysts (k_0) from k_{obs}; $k = k_{obs} - k_0$ [20,38]. The catalytic rate constants of nanocatalysts conducted at four

different reaction temperatures indicate that the catalytic performances of nanocatalysts increase rapidly with increment of temperature. Figure 2-6 and Table 2-1 exhibit that a certain period of time was required for a certain Ag/Au nanocatalyst to start catalysis. As observed in a number of systems [8,34-36], this period, defined as the induction time (t_0), has been attributed to a slow diffusion of reactants onto the catalytic surfaces. Table 2-1 indicates that the induction time is necessary for Ag/Au nanoboxes with hollow interiors, suggesting that the fast catalytic degradation of RhB molecules takes place in the cavities of Ag/Au nanoboxes and that it takes t_0 for RhB to diffuse through the walls of the nanoboxes. Table 2-1 also suggests that t_0 decreases gradually as the walls of the nanoboxes become more porous. Meanwhile, none of Ag_{pr}, Ag/Au_0, and Ag/Au_{105} show the induction time because none of them have hollow interiors.

Table 2-1. Observed rate constants (k_{obs}) at 25 °C, induction time (t_0) at 25 °C, activation energies (Ea), frequency factors (A), activation enthalpies ($\Delta H^{\ddagger}$), and activation entropies ($\Delta S^{\ddagger}$) for the catalytic reduction of RhB via nanocomposites in the presence of BH_4^-.

Catalyst	d_c[a] (nm)	k_{obs}[b] (min^{-1})	t_0 (min)	Ea (kcal mol^{-1})	A (min^{-1})	$\Delta H^{\ddagger}$ (kcal mol^{-1})	$\Delta S^{\ddagger}$ (cal mol^{-1} K^{-1})
Ag_{pr}	–[c]	0.0014	0	34.4	3.1×10^{21}	33.8	29.6
Ag/Au_0	–	0.035	0	28.0	1.2×10^{19}	27.4	18.5
Ag/Au_{25}	30	0.072	35	21.7	6.7×10^{14}	21.1	-0.9
Ag/Au_{55}	33	0.11	27	19.6	2.3×10^{13}	19.0	-7.2
Ag/Au_{85}	39	0.16	22	15.9	9.1×10^{10}	15.4	-18.6
Ag/Au_{105}	–	0.0016	0	32.9	5.0×10^{20}	32.3	26.0

[a] Average cavity diameters estimated using HRTEM images.
[b] The value in the absence of any catalysts (k_0) is 0.0012 min^{-1}.
[c] Not observed.

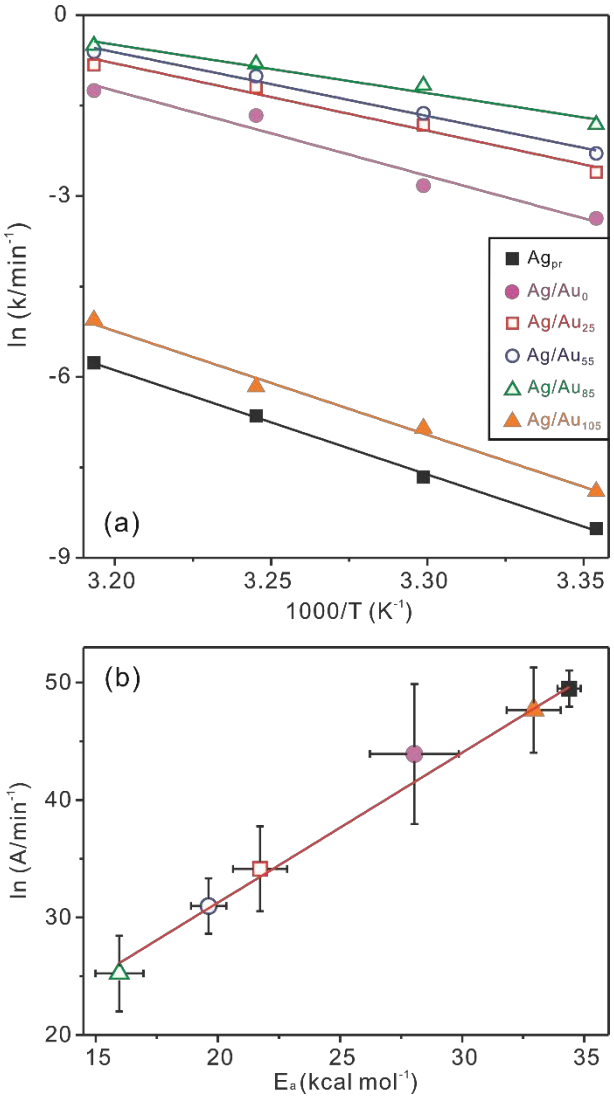

Figure 2-7. (a) Arrhenius plots for the catalytic reduction reaaction of 11 μM RhB(aq) via indicated nanocatalysts in the presence of 1.3 mM KBH_4. (b) The compensation law plot of the frequency factors and the activiation energies extracted from the Arrhenius plots.

Figure 2-7a shows that Arrhenius plots have been used to extract the activation energies (E_a) and frequency factors (A) of Ag_{pr} and Ag/Au nanocatalysts. Table 2-1

indicates that Ag/Au nanocatalysts with hollow interiors have much smaller E_a and A values than nanocatalysts without cavities. As already discussed with Figure 2-6, this observation also suggests that the catalysis reaction taking place in cavities is much faster than the reaction occurring at exterior surfaces as the confinement effect reduces the energy barrier. A close examination of Table 2-1 reveals that among Ag/Au nanoboxes having hollow structures, in particular, Ag/Au_{85} has the smallest E_a value to show the highest catalytic activity because the Ag/Au_{85} nanocatalyst has the largest nanocavity surrounded by the most porous walls. Furthermore, the activation enthalpies ($\Delta H^{\ddagger}$) and activation entropies ($\Delta S^{\ddagger}$) listed in Table 1 have been elicited from Eyring plots in Figure 2-S6: $\ln(k/T)$ vs $1/T$ to exhibit $\ln(k/T) = -\Delta H^{\ddagger}/(RT) + \Delta S^{\ddagger}/R + \ln(k_b/h)$ [37,38]. Table 2-1 shows that not only $\Delta H^{\ddagger}$ but also $\Delta S^{\ddagger}$ are smallest for Ag/Au_{85}, suggesting that the formation of the activated complex for the catalytic degradation reaction of RhB via Ag/Au_{85} is most favorable in energy but most unfavorable in degree of freedom. This suggests that the most efficient catalytic performance and the smallest E_a value of Ag/Au_{85} can be attributed to the energetically most favorable formation of the activated complex within the cavity of a Ag/Au_{85} nanobox. Overall, Figure 2-7a and Table 2-1 have revealed that the catalytic activity depends on the morphologies of Ag/Au nanocomposites, which can be controlled by adjusting the galvanic replacement temperature. In particular, Ag/Au_{85} that has been fabricated at 85 ^{o}C shows the most efficient catalytic performance.

Figure 2-7b shows the compensation law plot of $\ln A = \alpha + E_a/(RT_\theta)$, where α is a constant and T_θ is called the fictitious isokinetic temperature, at which the catalytic

rates of all the nanocomposites become the same [26,39,40]. The empirical linear relationship between ln A and E_a of Figure 2-7b clearly demonstrates the compensation effect in our catalytic system, where T_θ has been found as 395 K. The compensation effect is relevant to a switching in kinetics from a regime where the overall rate is controlled by the activation of the reactant to a regime where the stability of the product becomes more important [26,40]. Thus, we consider that for the reaction with Ag/Au nanoboxes having cavities, E_a was lower while the lower density of active sites would be compensated largely the stability of adsorption.

The catalytic reduction mechanism of RhB via nanocatalysts in the presence of KBH_4 could be described as follows. The nucleophilic BH_4^- ions supply electrons to Ag/Au nanocatalysts and then electrophilic RhB molecules adsorbed on Ag/Au nanocatalysts take electrons from Ag/Au nanocatalysts, facilitating electron transfer from BH_4^- to RhB through their catalytic surfaces [20,31,38]. Hence, Ag/Au nanocatalysts act as electron relays for the degradation reaction of RhB in the presence of KBH_4 [8,31,38]. With respect to the higher catalytic activity of Ag/Au nanoboxes, the nanoreactor confinement effect of Ag/Au nanocatalysts with hollow interiors is considered to expedite electron relays from BH_4^- to RhB enormously by reducing E_a extensively.

2. 5. Conclusion

Morphology-controlled Ag/Au nanocomposite have been fabricated facilely via a modified galvanic replacement reaction using Ag nanocubes as sacrificial templates. The morphologies of Ag/Au nanaocomposites have been readily controlled by adjusting the temperature of the galvanic reaction; the structures of Ag/Au nanocomposites prepared at 0, 25, 55, 85, and 105 ^{o}C are Au-decorated Ag nanocubes, well-defined nanoboxes, truncated nanoboxes, and porous nanoboxes, and broken nanoboxes, respectively. We have investigated the catalytic activities of Ag nanocubes and Ag/Au nanocomposites by monitoring the time-dependent reduction of RhB in the presence of KBH_4; Ag/Au nanocomposites with hollow interiors have shown much higher catalytic activity with a smaller activation energy than pristine Ag nanocubes or Ag/Au nanocomposites without cavities. Among Ag/Au nanoboxes having hollow structures, Ag/Au nanocomposites fabricated at 85 ^{o}C show the most efficient catalytic performances as their largest nanocavities are surrounded by the most porous walls. With respect to the higher catalytic activity of Ag/Au nanoboxes, the nanoreactor confinement effect of Ag/Au nanocatalysts with hollow interiors is considered to expedite electron transfer from KBH_4 to RhB enormously by reducing E_a largely; the energetically favorable formation of the activated complex within the cavities has lowered the energy barrier subsequently. Overall, the temperatures of galvanic replacement reactions have been varied to optimize the morphologies and the subsequent catalytic performances of Ag/Au nanocomposites.

2. 6. Acknowledgement

This work was supported by research grants through the National Research Foundation of Korea funded by the Korea government (2014-057382 and 2015-051798).

2. 7. Supporting information

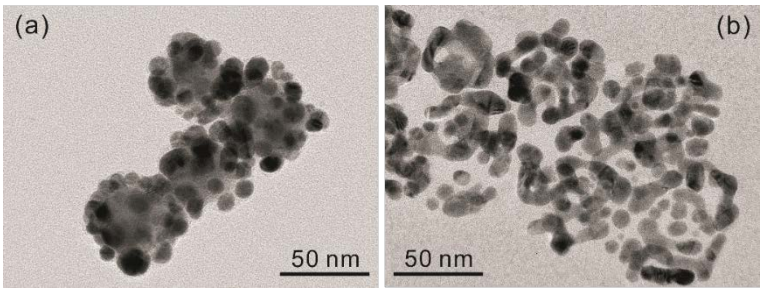

Figure 2-S1. TEM images of (a) Ag/Au_0 and (b) Ag/Au_{105}.

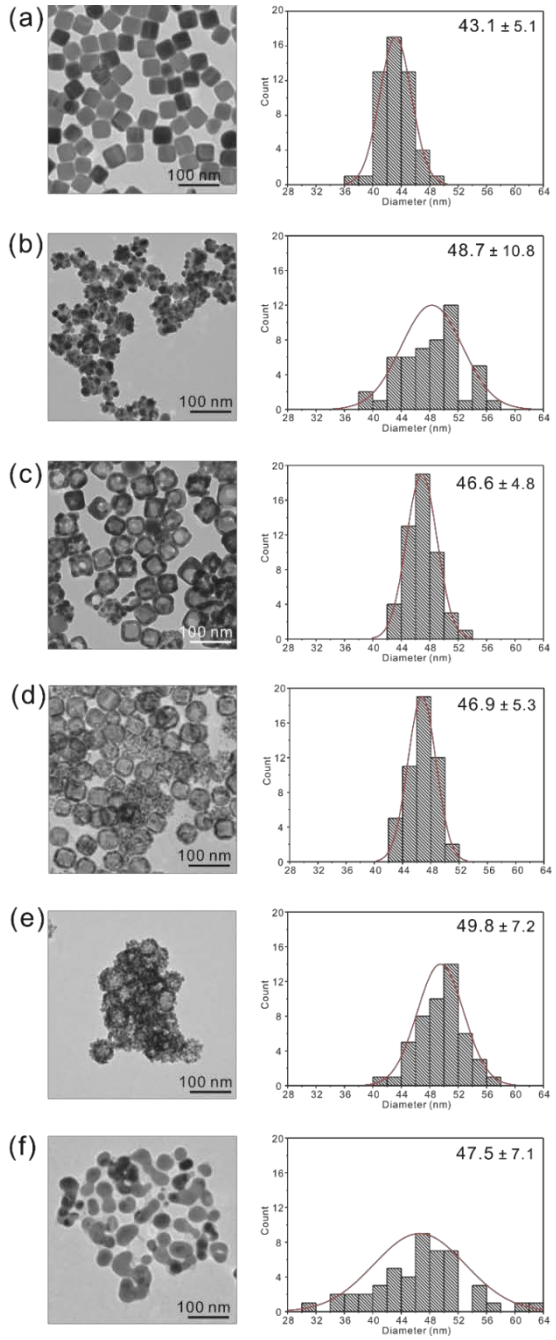

Figure 2-S2. TEM images and edge-size distribution histograms of (a) Ag_{pr}, (b) Ag/Au_0, (c) Ag/Au_{25}, (d) Ag/Au_{55}, (e) Ag/Au_{85}, and (f) Ag/Au_{105}. Average edge sizes are indicated inside the histograms.

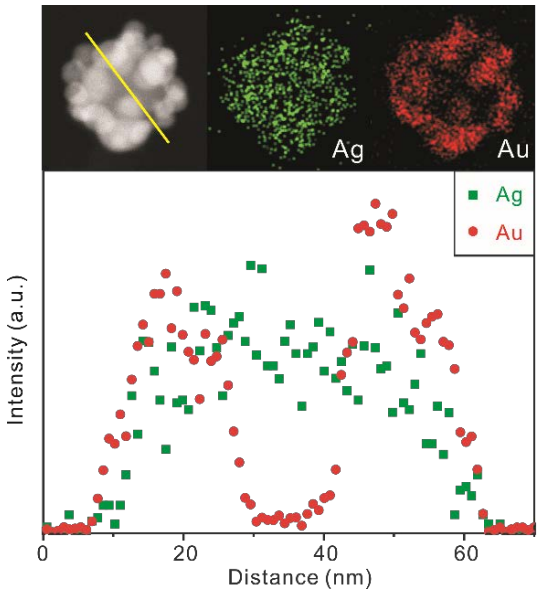

Figure 2-S3. STEM image, EDX elemental maps, and area-normalized line-scanned (along the line of the STEM image) elemental intensity profiles of Ag/Au_0.

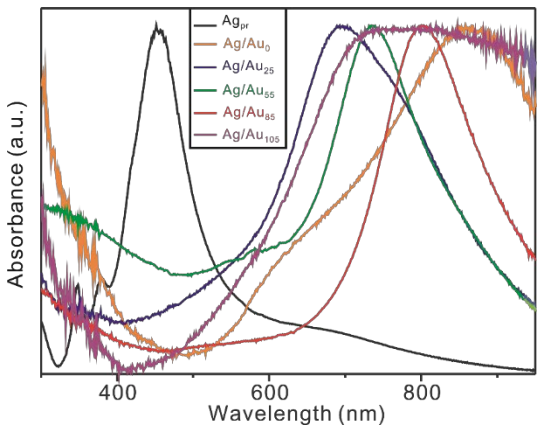

Figure 2-S4. Maximum-normalized surface-plasmon resonance spectra of indicated nanocatalysts in water.

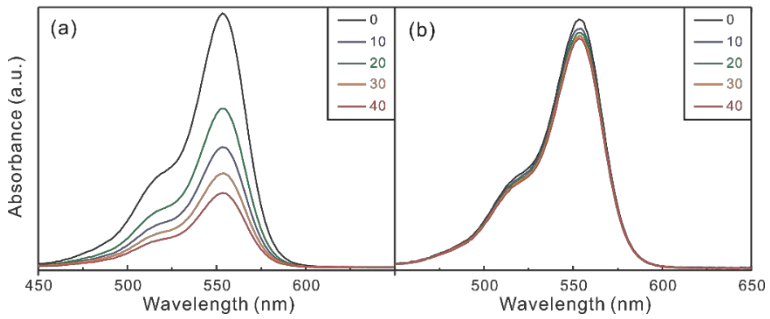

Figure 2-S5. Absorption spectra at 25 °C of 11 μM RhB(aq) in the presence of 1.3 mM KBH_4, measured at elapsed times indicated in the units of min after addition of (a) Ag/Au_0 and (b) Ag/Au_{105}.

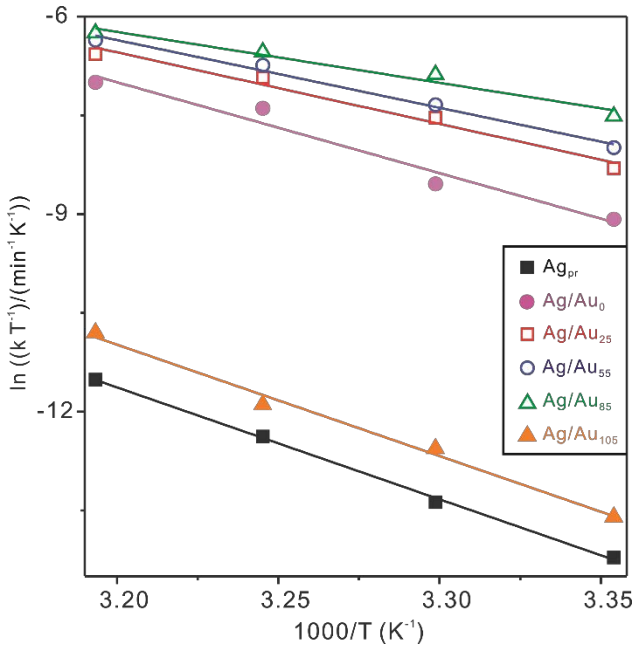

Figure 2-S6. Eyring plots for the catalytic degradation reaaction of 11 μM RhB(aq) via indicated nanocatalysts in the presence of 1.3 mM KBH_4.

2. 8. References

[1] G. Collins, J.D. Holmes, Adv. Mater. 28 (2016) 5689-5695.

[2] M. Salerno, J.R. Krenn, B. Lamprecht, G. Schider, H. Ditlbacher, N. Felidj, A. Leitner, F.R. Aussenegg, Optoelectron. Rev. 10 (2002) 217-224.

[3] L. Wang, Y. Yamauchi, J. Am. Chem. Soc. 135 (2013) 16762-16765.

[4] P.K. Jain, X. Huang, I.H. El-Sayed, M.A. El-Sayed, Acc. Chem. Res. 41 (2008) 1578-1586.

[5] M.R. Langille, M.L. Personick, J. Zhang, C.A. Mirkin, J. Am. Chem. Soc. 134 (2012) 14542-14554.

[6] Y. Yin, C. Erdonmez, S. Aloni, A.P. Alivisatos, J. Am. Chem. Soc. 128 (2006) 12671-12673.

[7] Y. Sun, B. Wiley, Z.-Y. Li, Y. Xia, J. Am. Chem. Soc. 126 (2004) 9399-9406.

[8] M. Son, J. Lee, D.-J. Jang, J. Mol. Catal. A-Chem. 385 (2014) 38–45.

[9] S. Duan, R. Wang, Prog. Nat. Sci. 23 (2013) 113–126.

[10] W. He, X. Wu, J. Liu, X. Hu, K. Zhang, S. Hou, W. Zhou, S. Xie, Chem. Mater. 22 (2010) 2988-2994.

[11] Q. Zhang, J. Xie, J. Liang, J.Y. Lee, Adv. Funct. Mater. 19 (2009) 1387-1398.

[12] P. Raveendran, J. Fu, S.L. Wallen, Green Chem. 8 (2006) 34-38.

[13] X. Xia, Y. Wang, A. Ruditskiy, Y. Xia, Adv. Mater. 25 (2013) 6313-6333.

[14] M.R. Kim, D.K. Lee, D.-J. Jang, Appl. Catal. B-Environ. 103 (2011) 253-260.

[15] F. Bellucci, Corrosion 47 (1991) 808–819.

[16] C. Yang, Q.B. Zhang, A.P. Abbott, Electrochem. Commun. 70 (2016) 60-64.

[17] E. González, J. Arbiol, V.F. Puntes, Science 334 (2011) 1377-1380.

[18] S.E. Skrabalak, J. Chen, Y. Sun, X. Lu, L. Au, C.M. Cobley, Y. Xia, Acc. Chem. Res. 41 (2008) 1587–1595.

[19] X. Gong, Y. Yang, S. Huang, J. Phys. Chem. C 114 (2010) 18073–18080.

[20] J.-A. Kwak, D.K. Lee, D.-J. Jang, Appl. Catal. B-Environ. 142-143 (2013) 323-328.

[21] J. Lee, K. Han, D.-J. Jang, Appl. Catal. A-Gen. 469 (2014) 380-386.

[22] M.A. Mahmoud, M.A. El-Sayed, Langmuir 28 (2012) 4051-4059.

[23] H. Zhang, M. Jin, J. Wang, W. Li, P.H. Camargo, M.J. Kim, D. Yang, Z. Xie, Y. Xia, J. Am. Chem. Soc. 133 (2011) 6078-6089.

[24] C.M. Kisukuri, D.J. Palmeira, T.S. Rodrigues, P.H.C. Camargo, L.H. Andrade, ChemCatChem 8 (2016) 171-179.

[25] X. Hong, D. Wang, S. Cai, H. Rong, Y. Li, J. Am. Chem. Soc. 134 (2012) 18165-

18168.

[26] J. Zeng, Q. Zhang, J. Chen, Y. Xia, Nano Lett. 10 (2010) 30-35.

[27] Q. Zhang, W. Li, L.-P. Wen, J. Chen, Y. Xia, Chem. Eur. J. 16 (2010) 10234-10239.

[28] M. Hu, H. Petrova, A.R. Sekkinen, J. Chen, J. M. McLellan, Z.-Y. Li, M. Marguez, X. Li, Y. Xia, G.V. Hartland, J. Phys. Chem. B 110 (2006) 19923-19928.

[29] S.E. Skrabalak, L. Au, X. Li, Y. Xia, Nat. Protoc. 2 (2007) 2182-2190.

[30] H. Wu, P. Wang, H. He, Y. Jin, Nano Res. 5 (2012) 135-144.

[31] J. Huang, S. Vongehr, S. Tang, H. Lu, J. Shen, X. Meng, Langmuir, 25 (2009) 11890-11896.

[32] F.H. AlHamedi, M.A. Rauf, S.S. Ashraf, Desalination, 239 (2009) 159-166.

[33] Y. Kim, H.-B. Kim, D.-J. Jang, J. Mater. Chem. A 2 (2014) 5791-5799.

[34] P. Herves, M. Perez-Lorenzo, L.M. Liz-Marzan, J. Dzubiella, Y. Lu, M. Ballauff, Chem. Soc. Rev. 41 (2012) 5577-5587.

[35] M.A. Mahmoud, M.A. El-Sayed, Nano Lett. 11 (2011) 946-953.

[36] S. Wunder, Y. Lu, M. Albrecht, M. Ballauff, ACS Catal. 1 (2011) 908-916.

[37] K.D. Zimmer, R. Shoemaker, R.R. Ruminski, Inorg. ChiM, Acta 359 (2006) 1478-1484.

[38] J. Lee, D.-J. Jang, J. Phys. Chem. C 120 (2016) 4130-4138.

[39] M.A. Mahmoud, F. Saira, M.A. El-Sayed, Nano Lett. 10 (2010) 3764-3769.

[40] T. Bligaard, K. Honkala, A. Logadottir, J.K. Nørskov, S. Dahl, C.J.H. Jacobsen, J. Phys. Chem. B 107 (2003) 9325-9331.

Appendicies

1. 1. List of Presentations

(1) **Hyeri Lee** and Du-Jeon Jang, "Laser-induced fabrication of hollow platinum nanospheres to have enhanced catalytic performances", *The 113th General Meeting of the Korean Chemical Society* Goyang, Korea (2014).

(2) **Hyeri Lee** and Du-Jeon Jang, "Preparation of Anatase TiO_2 Nanotube Arrays Dominated with Highly Energetic {001} Facets via Anodization", *The 115th General Meeting of the Korean Chemical Society* Goyang, Korea (2015).

(3) **Hyeri Lee** and Du-Jeon Jang, "Fabrication of Anatase TiO_2 Nanotubes with Highly Reactive Facets for High Photocatalytic Performances", *The 117th General Meeting of the Korean Chemical Society* Goyang, Korea (2016).

1. 2. List of Publications

(1) **Hyeri Lee**, Jin-Ah Kwak, and Du-Jeon Jang, "Observation and characterization of the surface plasmon resonances of platinum nanoshells", *Bull. Korean Chem. Soc*., **2014**, *35*, 945-948.

(2) **Hyeri Lee**, Jin-Ah Kwak, and Du-Jeon Jang, "Laser-induced fabrication of hollow platinum nanospheres for enhanced catalytic performances" *J. Phys. Chem. C*, **2014**, *118*, 22792-22798.

(3) **Hyeri Lee**, Tae-Hyeon Park, and Du-Jeon Jang, "Preparation of anatase TiO_2 nanotube arrays dominated with highly reactive facets via anodization for high photocatalytic performances", submitted to journal.

(4) Tae-Hyeon Park, **Hyeri Lee**, and Du-Jeon Jang, "Morphology evolution of Ag/Au nanocomposites via temperature-controlled galvanic exchange to enhance catalytic activity", submitted to journal.

Abstract (Korean)

나노 물질의 제조 방법, 특성 평가 및 촉매로의 응용에 대해 물리화학 및 재료화학 관점에서 연구하였다. 제 1장에서는 Ti foil을 기반으로 사용해 이차 양극 산화반응 통해 활성면이 노출이 증가된 아나타제 이산화티타늄 나노튜브 어레이 합성 연구 및 광촉매 매커니즘에 관한 연구를 기술하였다. 전해질 내의 플루오린 농도 및 양극 산화반응 시간의 길이 변화를 통해 이산화티타늄 나노튜브 어레이의 형태적, 결정 구조 및 표면의 활성면 노출 정도를 제어하고 이에 대한 광학적 특성 및 결정학적 특성을 확인하였다. 11시간 동안 양극 산화반응을 통해 합성한 아나타제 이산화티타늄 나노튜브 어레이 물질이 이산화티타늄 표면에 향상된 (004)면을 지님으로 인해 가장 활성화된 광촉매 반응효율을 나타냈다. 또한 이산화티타늄 표면의 (004)면에 의한 광촉매 반응 매커니즘 또한 라디칼 반응을 통해 연구하였다.

제 2장에서는 Ag nanocube를 template로 사용하여 갈바닉 치환반응을 통해 형태가 조절된 Ag/Au nanocomposite을 합성하였다. 갈바닉 치환반응 온도 조건을 조절함에 따라 상호확산 속도의 차이에 따라 다른 형태의 Ag/Au nanocomposite가 형성되었다. 합성된 나노물질들 중에서, 85 ºC에서 갈바닉 치환반응을 통해 합성된 나노물질이 가장 큰 공동 및 다공성 구조를 가지므로 인해 큰 촉매 활성이 나타났다. 갈바닉 치환반응의 온도를 조절하여 형태 최적화 및 이에 따른 촉매 활성에 대해 연구하였다.

주요어: 나노박스, 나노튜브 어레이, 동공 구조, 분해, 아나타제 이산화티타늄, 양극산화반응, 활성면

학번: 2013-22934